An integrated geochemical spatial and temporal survey of thermal springs to characterize the geothermal resource of a volcano (Piton des Neiges, Réunion Island)

Bhavani Bénard, Vincent Famin, Bernard Sanjuan, Françoise Vimeux, Bertrand Aunay, Pierre Agrinier, Geneviève Lebeau

HAL Id: hal-04125151

https://hal.univ-reunion.fr/hal-04125151v1

Submitted on 3 Dec 2023

Journal Pre-proof

An integrated geochemical spatial and temporal survey of thermal springs to characterize the geothermal resource of a volcano (Piton des Neiges, Réunion Island)

Bhavani Bénard, Vincent Famin, Bernard Sanjuan, Françoise Vimeux, Bertrand Aunay, Pierre Agrinier, Geneviève Lebeau

Please cite this article as: Bénard, B., Famin, V., Sanjuan, B., Vimeux, Franç., Aunay, B., Agrinier, P., Lebeau, Geneviè., An integrated geochemical spatial and temporal survey of thermal springs to characterize the geothermal resource of a volcano (Piton des Neiges, Réunion Island), *Applied Geochemistry* (2023), doi: https://doi.org/10.1016/j.apgeochem.2023.105689.

This is a PDF file of an article that has undergone enhancements after acceptance, such as the addition of a cover page and metadata, and formatting for readability, but it is not yet the definitive version of record. This version will undergo additional copyediting, typesetting and review before it is published in its final form, but we are providing this version to give early visibility of the article. Please note that, during the production process, errors may be discovered which could affect the content, and all legal disclaimers that apply to the journal pertain.

1 # An integrated geochemical spatial and temporal survey of thermal springs to

2 characterize the geothermal resource of a volcano (Piton des Neiges, Réunion

3 Island)

4 Bhavani Bénard[a, b, c], Vincent Famin[a, b], Bernard Sanjuan[c], Françoise Vimeux[d, e], Bertrand Aunay[f], Pierre

5 Agrinier[a], Geneviève Lebeau[a, b]

6 [a] Université de Paris, Institut de Physique du Globe de Paris, CNRS, F-75005 Paris, France

7 [b] Université de La Réunion, Laboratoire GéoSciences Réunion, F-97744 Saint Denis, France

8 [c] BRGM, F-45060 Orléans, France

9 [d] HydroSciences Montpellier (Univ. Montpellier, CNRS, IMT, IRD), UMR 5151, 34095 Montpellier,

10 France

11 [e] Institut Pierre Simon Laplace (IPSL), Laboratoire des Sciences du Climat et de l'Environnement (LSCE),

12 UMR 8212 (CEA, CNRS, UVSQ), 91191 Gif-sur-Yvette Cedex, France

13 [f] BRGM, F-97400 Saint-Denis, La Réunion, France

14 ## Highlights

15 The heat source of hydrothermal waters is one of the volcanic rift zones.

16 There are two independent hydrothermal reservoirs on the northern and southern sides of the

17 volcano.

18 Recharge of the two hydrothermal systems is plurennial and mostly fed by cyclones.

19 Geothermometry yields water-rock interaction temperatures of up to 141 ± 15°C.

20 The southern side of the volcano is the most promising target for future exploitation.

21 Coupling spatial and temporal geochemical information is useful for the geochemical exploration of

22 hidden geothermal systems.

23 ## Abstract

24 Geothermal exploration can be challenging in the absence of obvious surface indicators of a high

25 enthalpy geothermal resource such as geysers, fumaroles or thermal springs with temperatures near

26 100°C. This is the case at the Piton des Neiges volcano (Réunion Island), which displays evidence of

27 hydrothermal activity mostly as thermal springs with temperatures not exceeding 50°C, affected by

28 mixing and reequilibration, and emerging in a complex geological framework, resulting from the

29 polygenic history of this dormant volcano. Yet, these thermal springs keep a partial record of the

30 reservoir geochemistry. Here, we propose an exploration method to set this thermal signature apart

31 from the contribution of other processes and trace back the equilibrium conditions, enabling us to

32 locate thermal fluid circulations, and evaluate their temperature and availability. We report its

33 application at Piton des Neiges volcano. We led an extensive geochemical survey which nearly doubled

34 the number of thermal springs reported on the volcano and dramatically extended the existing

35 geochemical database in space and time. In tandem, we also monitored $\delta^{18}O$ and δD values in

36 rainwaters and thermal springs over two years to compare their temporal variations.

1

37 Our surveys show that the repartition of thermal springs is controlled by only one of the volcanic rift
38 zones (the N30°E axis), which is thus identified as the heat source of hydrothermal circulations. This
39 N30°E rift zone is also a preferential pathway for the degassing of mantellic CO_2. In addition, the
40 composition of thermal waters is influenced by syenite intrusions along the rim of the caldera, acting
41 as drains for the uprise of hydrothermal waters. O, H and Sr isotopic signatures of springs show that
42 the geothermal resource of Piton des Neiges is in fact made of two independent and unconnected
43 hydrothermal systems on the northern and southern circular depressions of the volcano (the cirques
44 of Salazie and Cilaos, respectively). Their recharge is meteoric, multi-year, and mostly achieved by
45 cyclonic events. Thermal waters experience reequilibration during their ascent and various degrees of
46 CO_2 input or degassing. Last equilibrium temperatures of water/rock interaction, estimated by
47 multicomponent geothermometry, reach up to 125 ± 6°C in the cirque of Salazie, and up to 141 ± 15°C
48 in the cirque of Cilaos, with possibility for hotter waters before reequilibration. Taken together, our
49 results suggest that the most promising target for future exploration is located in the cirque of Cilaos,
50 along the caldera rim, and in proximity of syenite intrusions.

51 With a thorough prospecting of thermal springs, a comprehensive geochemical study and a
52 geochemical monitoring of the different water reservoirs, we improved our understanding of the
53 geothermal resource and identified future exploration targets at Piton des Neiges volcano.

Keywords

55 Geothermal ; Exploration ; Geochemistry ; Piton des Neiges ; Volcano ; Thermal springs

Introduction

57 Geothermal energy is a renewable energy source with little emission of carbon dioxide to the
58 atmosphere and thus well suited to climate change mitigation. However, geothermal exploration can
59 be challenging in the absence of obvious surface indicators of a high enthalpy geothermal resource
60 such as geysers, fumaroles or thermal springs with temperatures near 100°C. Yet, these "hidden"
61 systems can represent the majority of the geothermal potential resource (e.g. in the U.S.A., Williams
62 et al., 2009). In order to address this issue, several methods are in development to assess their
63 geothermal potential such as statistical analysis (e.g. in Hawaii, Lautze et al., 2017b, 2017a), machine
64 learning (e.g. in the U.S.A., Vesselinov et al., 2021), or 3D magnetotelluric surveys (e.g. in La Palma,
65 Canaries, Di Paolo et al., 2020). Most of the time, these systems still display some evidence of
66 hydrothermal activity, often in the form of non-boiling thermal waters, which can represent a
67 supplementary exploration tool. This type of manifestation is especially common on mature and
68 polygenic volcanoes, for example as groundwaters with thermal anomalies in the islands of Maui and
69 Lanai, Hawaii (Lautze et al., 2017a), or as thermal springs on the Taburiente volcano in La Palma,
70 Canaries (Troll and Carracedo, 2016) and in Quaternary and Tertiary formations of western Iceland
71 (Arnórsson, 1995). However, polygenic volcanoes are by essence made of multiple eruptive periods,
72 quiescent phases and destabilization episodes. This history results in complex internal architectures,
73 which affect the geometry of thermal water circulation as well as the location, depth, and nature of
74 the heat sources and the permeability of rocks (e.g. at Mount Meager in British Columbia, Grasby et
75 al., 2019), making the use of thermal springs for geothermal exploration challenging.

76 Réunion Island is a good example of a polygenic volcanic island offering potential for geothermal
77 energy, but where exploitation is hampered by a lack of geological knowledge on the hydrothermal
78 systems (see review by Dezayes et al., 2022). Piton des Neiges volcano displays evidence of
79 hydrothermal activity, in the form of thermal springs (up to 48°C), fumarole deposits, and CO_2 – He –

80   Rn anomalies (Marty et al., 1993; Rançon and Rocher, 1985; Sanjuan et al., 2001). This volcano also
81   hosts several geophysical indicators in favor of a geothermal resource (Dezayes et al., 2022). Moreover,
82   two exploratory boreholes revealed the existence of elevated temperature gradients (180°C/km and
83   82°C/km) on this dormant volcano. All these lines of evidence confirm the presence of a heat source
84   and of hot water circulation, which may be suitable for the development of geothermal energy on the
85   island. However, exploratory drillings made so far did not reach zones of sufficient permeability to
86   allow an exploitation of hot water (Augé et al., 1989; Demange et al., 1989). More geological
87   information is needed to locate fluid circulations in this dormant volcano, assess the resource
88   represented by its hydrothermal system, and define the most promising targets for future exploration.

89   In a previous paper, we proposed a conceptual model for the Piton des Neiges hydrothermal system
90   in a first study (Bénard et al., 2020). Based on the chemical and isotopic composition of 17 thermal
91   springs, we determined the different mineralization processes responsible for their geochemical
92   profiles. We found that thermal waters are of meteoric origin, subject to CO_2 dissolution from a
93   degassing magma, to water-rock interaction with either basalts or differentiated rocks which increase
94   their total mineral content, and some samples also showed a contamination from elements originating
95   from seawater. With the knowledge of the processes involved in the mineralization of thermal waters,
96   the aim of the present work is to characterize the geothermal resource and estimate its temperature.
97   For this purpose, we led an extended field prospection and sampling, which includes waters displaying
98   field evidence of a thermal component and rocks from different geological units. We used
99   physiochemical parameters, major element concentrations, and CO_2 partial pressure (PCO_2)
100   computations to highlight the zones displaying the most promising geothermal resource. In order to
101   better understand the hydrogeological characteristics of the aquifer systems with which thermal
102   waters are mixed, we studied the spatial distribution of Cl, $\delta^{18}O$ and δD in waters and that of $^{87}Sr/^{86}Sr$
103   in waters and rocks. To refine our understanding of aquifer recharge, we monitored the monthly
104   isotopic composition ($\delta^{18}O$, δD) of rain and thermal springs over two years. We then applied the most
105   up-to-date thermodynamic-based geothermometry tools (Cioni and Marini, 2020; Spycher and
106   Finsterle, 2016) to reconstruct the temperature history of the geothermal fluids. This work leads to a
107   considerably improved model of hydrothermal circulation at Piton des Neiges, which may be used to
108   target zones where the geothermal resource is most likely present and to plan the next steps of
109   geothermal exploration. Our methodology of geochemical investigation may be exported to any other
110   volcano with thermal springs mixing with superficial waters.

111   1. Geological and hydrogeological settings

112   Réunion Island was formed by two main volcanoes: Piton des Neiges and Piton de la Fournaise. Piton
113   des Neiges, presently dormant, is the oldest and the largest edifice. Piton de la Fournaise, still active,
114   grows on the south-eastern flank of Piton des Neiges. Estimated to have emerged at 3 Ma ago, Piton
115   des Neiges has a polygenic history of at least five eruptive periods separated by quiescence and erosion
116   intervals. The shield building stage of this volcano has produced transitional basic magmas until 430
117   ka (Kluska, 1997; McDougall, 1971). After a 80 ka period of rest, the volcano entered into a
118   degenerative stage 350 ka ago and produced alkali differentiated magmas ever since (Gillot and
119   Nativel, 1982; Kluska, 1997). The last known eruption of Piton des Neiges dates back to 27 ka (see
120   review by Famin et al., 2022). This last period of quiescence, and the heavy rainfalls under tropical
121   climate, have favored erosion of the volcanic edifice, now incised by three cirques (subcircular
122   depressions), Salazie to the north, Mafate to the northwest, and Cilaos to the south (Figure 1). These
123   deep cirques have dissected the inner structure of the volcano, erasing most of the surface evidence
124   of calderas. Based on patchy observations of faults, offset lava layers, pyroclastic deposits or radial
125   dykes, two calderas have been proposed (Figure 1): a large one running through the three cirques

126 formed during the differentiated stage (210 – 180 ka), and a smaller one in the summit area of Piton
127 des Neiges formed during its last activity (Chevalier, 1979; Rocher, 1988).

128 Erosion has exposed the hypovolcanic complex, made of dense gabbroic plutons and basaltic, trachytic
129 and syenitic planar intrusions. Planar intrusions are organized into two rift zones N30°E and N110-
130 160°E, and two sill zones between 800 and 1300 m above sea level (Chaput et al., 2017, 2014). The
131 two deep boreholes SGTH-1 (201 m) and SLZ1 (2108 m) drilled for geothermal exploration in the 1980s
132 (Chovelon, 1986; Gérard and Stieltjes, 1979) intersect a pluri-kilometric gabbroic intrusive complex,
133 associated with the shield building stage of Piton des Neiges. The high geothermal gradients
134 (respectively of 180°C/km and 82°C/km) obtained in these boreholes show that heat issued from
135 volcanic activity is still being transmitted into the massif. However, both boreholes were dry and the
136 nature of the heat source (either the gabbro pluton or the planar intrusions) remains unknown. Syenite
137 intrusions, which consist in 30 – 100 m thick dykes in the cirques of Salazie and Cilaos, are of particular
138 interest for this study. Ages of less than 150 ka, they represent major dyke structures of the terminal
139 volcanic activity (Famin et al., 2022), located within the N30°E rift zone, and interpreted to delineate
140 the largest caldera (Chevalier, 1979; Rocher, 1988). Additionally, many thermal springs are observed
141 in these intrusions or in their immediate vicinity. All these criteria suggest that syenite intrusions
142 represent a candidate heat source for the hydrothermal system, or at least act as conduits for hot fluid
143 flow (Bénard et al., 2020; Frissant et al., 2003; Sanjuan et al., 2001).

144 Fluid circulation in the edifice is complexified by its long history of construction, destruction, intrusive
145 activity and secondary mineral precipitation. Indeed, the hypovolcanic complex of Piton des Neiges is
146 affected by several phases of low-grade metamorphism and hydrothermal alteration (Chevalier, 1979;
147 Rançon, 1985), resulting in a porosity clogging by secondary precipitation of phrenite-pumpellyite
148 facies minerals in rocks of the shield-building stage, followed by carbonate precipitation in
149 differentiated rocks as well as in mafic rocks (Famin et al., 2016). The ensued low hydraulic
150 conductivity, associated with the geological barriers formed by planar intrusions, limit the escape of
151 freshwater toward the sea and its downward infiltration in the lowermost, oldest and most
152 impermeable rock units (Join et al., 2005). Thermal waters, accordingly, is mostly fed by meteoric water
153 (Bénard et al., 2020). The tropical climate of Réunion Island consists in a dry season (April-November),
154 and a wet season (December-March) that delivers huge precipitation rates (annual mean of ~2500 mm
155 in the cirques). Most of these wet season rainfalls occur as cyclones or tropical storms (five events per
156 year in average for the period 1981 – 2010; Jumaux et al., 2011).

157 Despite the present-day inactivity of Piton des Neiges, there is still evidence of magmatic degassing
158 from a deep mantle source on a regional scale (Boudoire et al., 2017). Magmatic carbon dissolves in
159 large quantities in the hydrothermal system (Bénard et al., 2020; Marty et al., 1993; Trull et al., 1993).
160 Fumarolic sulfur deposits are also observed, but it is unknown whether they are fossil or still active
161 (Lopoukhine and Stieltjes, 1978; Rançon and Rocher, 1985).

4
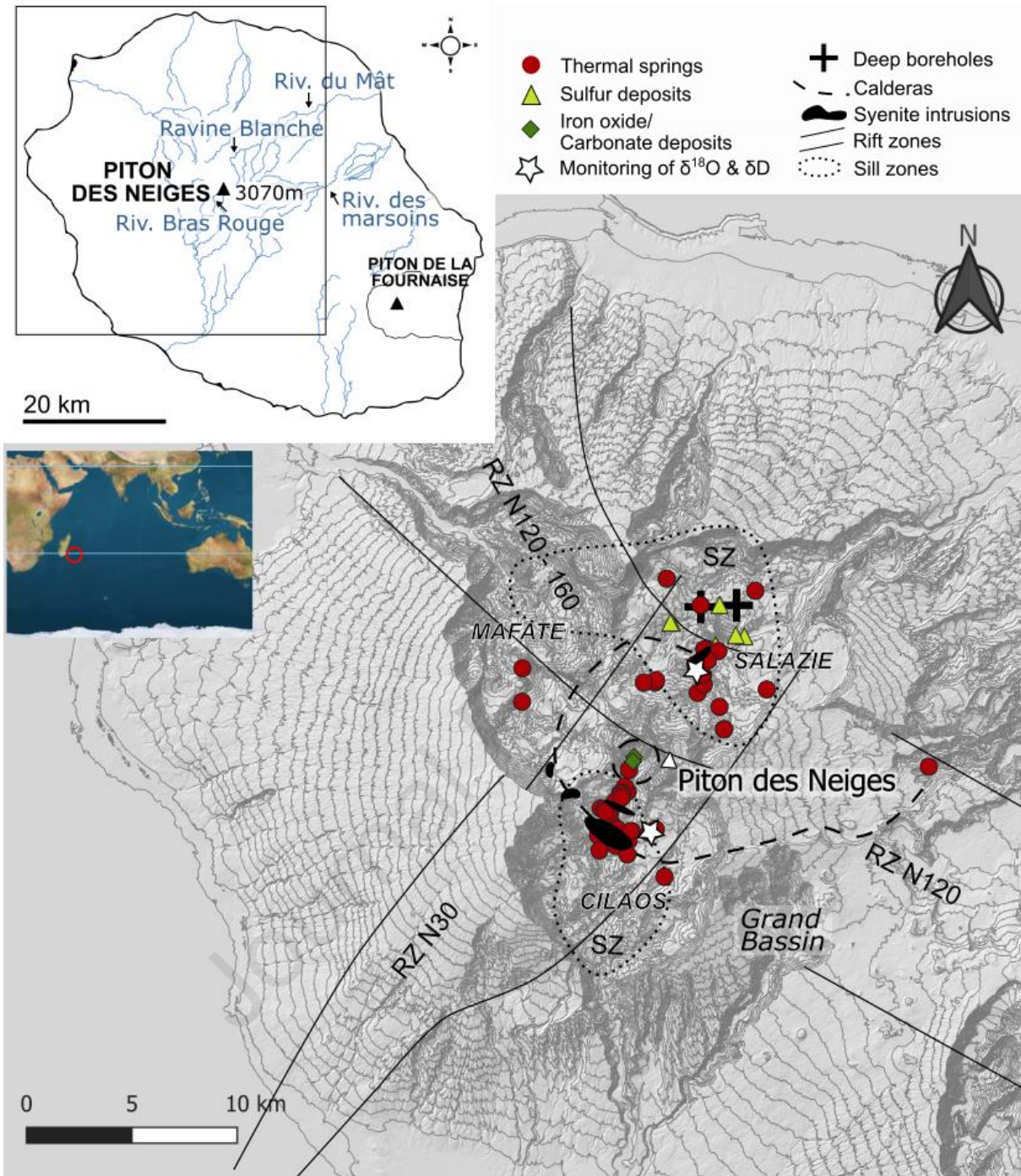
162

163 Figure 1: Localization of the field indicators of hydrothermal activity in Piton des Neiges: thermal springs, iron oxide
164 deposits, carbonate deposits and sulfur deposits from previous studies (Aunay et al., 2013; Belle, 2014; Bénard et
165 al., 2020; Frissant et al., 2003; Iundt et al., 1992; Lopoukhine and Stieltjes, 1978; Louvat and Allègre, 1997;
166 Sanjuan et al., 2001), the main rift zones (RZ) and sill zones (SZ) of Piton des Neiges (Chaput et al., 2017), the
167 two supposed calderas (Chevalier, 1979; Rocher, 1988), the two deep boreholes drilled for geothermal exploration
168 in the 1980s (Chovelon, 1986; Gérard and Stieltjes, 1979), the two monitoring sites of $\delta^{18}O$ and δD in springs and
169 rain. Relief contours at 100 m intervals from RGE ALTI® - IGN.

2. Material and Methods

2.1. Fieldwork and sampling

5

172   We led an extensive prospection on the field to identify all indicators of hydrothermal activity and
173   measure and sample new thermal springs. Springs were considered as an indicator of
174   hydrothermal activity whenever they displayed at least two of the following criteria:

175   -   Presence of iron oxide/carbonate/sulfide deposits,
176   -   A higher temperature (≥ 5°C) compared to nearby river water at the time of sampling,
177   -   A higher electrical conductivity (EC) (≥ 200 µS/cm) compared to nearby river water at the time
178   of sampling,
179   -   A lower pH (≤ 1) compared to nearby river water at the time of sampling.

180   Temperature, EC, and pH were measured at the outlet and EC was normalized at 25°C.

181   In total, our spatial and temporal sampling campaign yielded a set of 130 water samples. The first
182   spring samples were taken during an exploratory phase in June 2015, hereafter referred to as "the first
183   phase". All the others spring samples were taken over a long period lasting from December 2015 to
184   May 2019, hereafter referred to as "the second phase".

185   Thermal springs were sampled to be analyzed for major elements, Al, Sr, and Br concentrations and
186   $\delta^{18}O$, δD, $\delta^{13}C$ and $^{87}Sr/^{86}Sr$ isotopic ratios. Thermal springs displaying particularly interesting or
187   intriguing features were sampled several times. The three large rivers Bras Rouge in Cilaos, Rivière du
188   Mât and Ravine Blanche in Salazie were also sampled at the highest possible altitude for analysis of
189   $\delta^{18}O$ and δD isotopic ratios in order to give reference points for river waters, respectively at 2050, 1830
190   and 1739 m. We also sampled several rocks from the late activity of Piton des Neiges – and thus the
191   most likely to produce heat – in order to compare their strontium isotopic signature to that of thermal
192   springs.

193   For all the samples, water was filtered at 0.2 µm on site. Bottles were rinsed three times with filtered
194   water before sampling. Bottle caps were sealed with parafilm. For the analysis of major and trace
195   elements, and $^{87}Sr/^{86}Sr$ isotopic ratios, water samples were collected in LDPE bottles. Water samples
196   for analysis of major cations, Al, Sr, and Br concentrations and $^{87}Sr/^{86}Sr$ isotopic ratios were acidified
197   with acid (HNO$_3$ 0.3N) on site. However, for the samples of the second phase, there was too little acid
198   to prevent calcite precipitation in the bottles, which resulted in erroneous values for the
199   concentrations of Ca and Sr for 17 samples, which were displayed in Bénard et al., (2020). For the
200   purpose of this study, we added back acid to unused samples from the second phase and re-analyzed
201   them for cations and trace elements. For $\delta^{18}O$ and δD analyses, water was sampled 15 mL amber glass
202   or HDPE bottles with no headspace. During the second phase, water samples were also collected for
203   analysis of total dissolved inorganic carbon content (TDIC) and $\delta^{13}C$ in Labco 12 mL Exetainer vials with
204   no headspace.

205   Additionally, we monitored rainwater and thermal springs time fluctuations on two sites from April
206   2017 to May 2019. On a monthly basis, we collected water from two thermal springs in each cirque
207   (Trou Blanc Amont – TBA – in Salazie and Irénée – IRN – in Cilaos, Figure 1) and from rainwater
208   collectors installed nearby these two springs (at elevations 910 m and 1120 m respectively) for analysis
209   of $\delta^{18}O$ and δD isotopic ratios. Springs IRN and TBA were also analyzed for major and trace elements.
210   These two springs were selected because of (i) their unambiguous hydrothermal signature (Bénard et
211   al., 2020), (ii) their relatively easy access, and (iii) the possibility of installing rainwater collectors
212   nearby. For the two rain collectors, rainwater was collected in a PEHD container through a funnel and
213   trapped under a layer of liquid paraffin to prevent water evaporation. Each month, one sample was
214   taken out of the total volume of water collected in a 15 mL bottle, made of amber glass with a cone-
215   shaped cap or of HDPE with no headspace. As for thermal springs, water was filtered at 0.2 µm on site,

6

216 bottles were rinsed three times with filtered water before sampling and bottle caps were sealed with
217 parafilm.

218 All the samples were stored at a temperature of 6°C before shipment.

219   2.2. Analysis

220 For the water samples of the first sampling phase, alkalinity, major/trace elements and $\delta^{18}O$, δD and
221 $^{87}Sr/^{86}Sr$ isotopic ratios' analyses were performed at the Bureau de Recherches Géologiques et
222 Minières (BRGM) in Orléans (France). For the water samples of the second sampling phase, total
223 dissolved inorganic carbon (TDIC) and major elements analyses were performed at the Institut de
224 Physique du Globe de Paris (IPGP). $\delta^{18}O$ and δD of thermal springs and precipitations were analyzed at
225 the Laboratoire des Sciences du Climat et de l'Environnement (LSCE) in Saclay. Sr concentrations and
226 isotopic ratios analyses on rocks were performed by the Service d'Analyse des Roches et des Minéraux
227 (SARM-CRPG) in Nancy.

228 Major anions concentrations were determined by ion exchange chromatography (ICS1100
229 Thermofisher, column Ionpac thermo AS14 and precolumn Ionpac thermo AG14, column AS14 and
230 precolumn AG14). Major cations concentrations were determined using inductively coupled plasma
231 atomic emission spectrometry (ICP-AES, iCAP6200 Thermofisher). For the Ca and Sr concentrations of
232 the 17 samples for which the previous analysis was inaccurate, we performed a new analysis using
233 inductively coupled plasma mass spectrometry (ICP-MS, Agilent 7900). Al, Sr, and Br concentrations
234 were determined by ICP-MS for the two phases. Precision for major cations and anions concentrations
235 is < 5 % (except HCO_3, < 10 %, see below), and < 20 % for trace elements. Uncertainties were calculated
236 using the standard deviation on measurement replicates and the uncertainty on the internal standard
237 concentration.

238 For the water samples of the first phase, alkalinity was determined using potentiometric titration,
239 giving HCO_3 concentrations with a quantification limit of 10 mg/L. For the water samples of the second
240 phase TDIC and carbon isotope ratios $\delta^{13}C$ analyses were made by gas chromatography and isotope
241 ratio mass spectrometry (GC-IRMS), after releasing TDIC as CO_2 by H_3PO_4 acidification (Assayag et al.,
242 2006). For this phase, HCO_3 concentrations were computed using the temperature dependent acid
243 dissociation constants from Mook and Koene, (1975), knowing the TDIC, temperature and pH of
244 waters. However, this analysis method gave poor estimates of dissolved carbonate concentrations for
245 the thermal springs with a high TDIC as 35 samples from the second phase yielded ionic balances >
246 5 %. For these 35 samples, HCO_3 concentrations had to be corrected and were estimated by setting
247 the ionic balance to 0 %. $\delta^{13}C$ are expressed in per mil (‰) with respect to the PDB standard, with a
248 precision of 0.1 ‰.

249 For the water samples of the first phase, $\delta^{18}O$ and δD of thermal spring and rivers were obtained by
250 gas chromatography coupled to isotope ratio mass spectrometry (GC-IRMS), after equilibration with
251 H_2 for hydrogen and CO_2 for oxygen, leading to an accuracy of 0.1 ‰ in $\delta^{18}O$ and 0.8 ‰ in δD. For the
252 water samples of the second phase, $\delta^{18}O$ and δD were obtained using the CO_2-H_2O equilibration
253 method on a Finnigan Mat 252 and the WS-CRDS infrared laser method respectively. $\delta^{18}O$ and δD are
254 expressed in ‰ with respect to the VSMOW standard. The accuracies are of ± 0.05 ‰ and ± 0.7 ‰ for
255 $\delta^{18}O$ and δD, respectively.

256 For the water samples of the first phase, $^{87}Sr/^{86}Sr$ ratios were determined by mass spectrometry using
257 a triple multidynamic acquisition and a single W filament. For the water samples of the second phase,

7

258 strontium isotopic ratios $^{87}Sr/^{86}Sr$ were determined by multi-collector mass spectrometry (TIMS).
259 Precisions are between 0.000006 and 0.000018.

260 Strontium isotopic ratios in rocks were determined by the Service d'Analyse des Roches et des
261 Minéraux (SARM) of the Centre de Recherches Pétrographiques et Géochimiques (CRPG), Nancy,
262 France. About 100 to 200 mg of sample were weighed in a 15 ml Savillex and digested using a solution
263 of 14M HNO_3 (4 mL). The whole mixture was heated on a hot plate at 115°C for 24 - 48 h, evaporated
264 to dryness and dissolved in 6M HCl and heated again for 24 h. After complete dissolution and
265 subsequent evaporation, the residue was diluted in 2 mL of 2 M HNO_3. Sr, Rb and REE were separated
266 using the Sr spec and Tru Spec resins (Pin et al., 1994). The Sr cuts were loaded onto Re filaments and
267 analyzed by TIMS Triton Plus (Thermo electron) in static multicollection. The $^{87}Sr/^{86}Sr$ ratios were
268 normalized to a $^{86}Sr/^{88}Sr$ ratio of 0.1194. Repeated analysis of the NBS 987 standard yielded an average
269 of 0.710255 ± 0.000017.

3. Results

271 Our field prospection highlighted 118 new surface indicators of hydrothermal activity to the already
272 71 reported in previous studies (Aunay et al., 2013; Belle, 2014; Bénard et al., 2020; Frissant et al.,
273 2003; Iundt et al., 1992; Lopoukhine and Stieltjes, 1978; Louvat and Allègre, 1997; Manès, n.d.; Marty
274 et al., 1993; Poul, 1966; Rocher, 1988; Sanjuan et al., 2001). Their coordinates and description and the
275 physiochemical parameters of the springs are given in Supplementary Material. We observed and
276 measured 28 out of the 71 indicators from previous studies, and found that 9 more have since
277 disappeared in landslides. Out of the total 189 field indicators, 28 are dry iron oxide/carbonate/sulfide
278 dry deposits and 161 are thermal springs. Thermal springs temperatures range from 9.8 to 48°C,
279 electrical conductivities range from 194 to 3370 µS/cm and pH range from 5.3 to 9.4. Mean values are
280 1050 ± 512 µS/cm for electrical conductivity, 6.9 ± 0.7 for pH and 20.8 ± 4.6°C for temperature. These
281 wide ranges of physiochemical parameters reflect the variability of the contribution of the
282 hydrothermal component to the geochemistry of the springs.

283 Major elements and Al, Sr, and Br concentrations were analyzed on 38 thermal springs (Table 1. For
284 our study, we included analyses of thermal springs from previous studies (Aunay et al., 2013; Belle,
285 2014; Frissant et al., 2003; Iundt et al., 1992; Lopoukhine and Stieltjes, 1978; Louvat and Allègre, 1997;
286 Sanjuan et al., 2001). For a comprehensive compilation of this literature data, see appendix A and B in
287 Bénard et al., (2020). On a Piper diagram, most springs gather at the HCO_3 end in the anion triangle
288 plot, and only a few springs tend toward the SO_4 or Cl ends (Figure 2). Therefore, most thermal springs

8

289   of Piton des Neiges can be considered bicarbonate waters. In the cation plot, some springs show a
290   trend towards the Na+K pole in the cation plot but most plot in the middle.
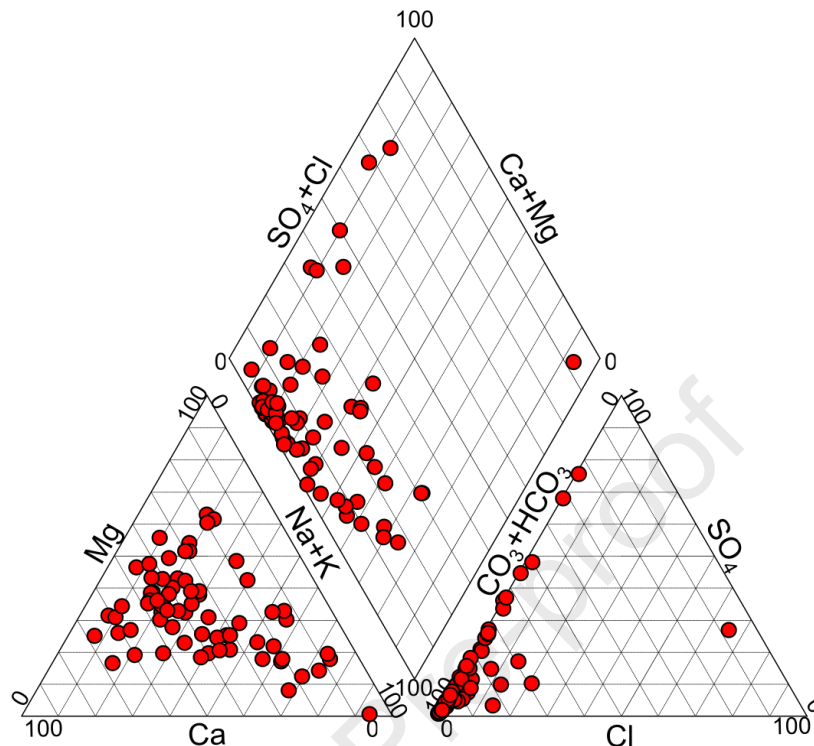
291

292   Figure 2: Piper diagram of thermal springs of Piton des Neiges. The composition of each thermal spring is the mean
293   of all the available data from this study and the literature.

294   Springs for which several analyses are available over the years show very little variation of their
295   geochemical composition. Their relative proportions of major elements display little variation over
296   time (1 s.d. of Na + K, Ca + Mg, SO_4+Cl, HCO_3 mole fractions ≤ 8 %) with the exception of TR and OLIVbis.

297   The results of $\delta^{13}C$, $\delta^{18}O$ and δD analyses in thermal springs are presented in Table 1. $\delta^{13}C$ values range
298   between -14.8 and 5.2 ‰. When considering the mean value of each spring, $\delta^{18}O$ and δD values for all
299   thermal springs range from -8.58 to -5.4 ‰ and from -58.8 to -23.5 ‰, respectively. Additionally,
300   surface water samples measured in rivers (Rivière Bras Rouge rBRO), Rivière du Mât (rRMA) and Ravine
301   Blanche (rRBL) yielded $\delta^{18}O$ and δD values of -7.18 and -44.4 ‰, -7.97 and -51.3 ‰, and -7.26 and -
302   46.1 ‰, respectively. These values are in the upper range of those measured in thermal springs.

303   Results of monthly monitoring of $\delta^{18}O$ and δD in rainwaters and thermal springs in the cirques of
304   Salazie and Cilaos are presented in Table 2. Over the sampled period, the $\delta^{18}O$ and δD of the thermal
305   springs TBA and IRN show almost no variation ($\delta^{18}O$=-6.81 ± 0.16 ‰ and δD=-40.2 ± 0.5 ‰ for TBA;
306    $\delta^{18}O$=-8.08 ± 0.06 ‰ and δD=-51.2 ± 0.23 ‰ for IRN). In contrast, rainwaters exhibit a wide range of
307    $\delta^{18}O$ and δD values, from -7.22 to -1.49 ‰ and -47.3 to +3.2 ‰ for Salazie, respectively, and from -
308   9.68 to -1.31 ‰ and -66.3 to +4.4 ‰ for Cilaos, respectively.

309   Analyses of strontium isotopic ratios are presented in Table 1 for thermal springs and Table 3 for rocks.
310   The $^{87}Sr/^{86}Sr$ ratios of Piton des Neiges thermal springs (0.704129 to 0.704364) are in the range of rocks
311   values from Salazie and Cilaos (0.704041 to 0.704504, Table 3). Our new analyses of trachyte and
312   syenite rocks display low $^{87}Sr/^{86}Sr$ ratios (0.704156 to 0.704215), in agreement with literature data
313   available for these types of rocks (0.704153 to 0.704268, mean 0.704181, Nauret et al., 2019;
314   Smietana, 2011).

9

315 Table 1: Physicochemical parameters, major elements concentrations, δ^{18}O, δD, δ^{13}C and ^{87}Sr/^{86}Sr isotopic ratios in thermal springs of Piton des Neiges.

Spring	Location	Date dd/mm/yyyy	Electrical Conductivity (µS/cm)	pH	Temperature (°C)	Ca (mmol/L)	Mg (mmol/L)	Na (mmol/L)	K (mmol/L)	HCO$_3$ (mmol/L)	SO$_4$ (mmol/L)	Cl (mmol/L)	SiO$_2$ (mmol/L)	Br (µmol/L)	Al (µmol/L)	Sr (µmol/L)	δ^{18}O (‰ VMOW)	δD (‰ VMOW)	^{87}Sr/^{86}Sr	δ^{13}C (‰ PDB)
AGS*	Salazie	17/06/2015	1746	6.5	21.1	6.75	3.49	1.65	0.1	14.52	4.11	0.03	1.28		0.0					
BACH*	Salazie	15/06/2015	1260	6.9	25.6	2.85	2.58	3.94	0.12	14.38	0.14	0.07	1.33		0.1		-6.7	-41.6	0.704317	1.4
BB*	Cilaos	05/05/2017	1699	6.7	25.1	3.96**	3.29	5.89	0.11	15.48**	2.32	0.39	1.99	0.43	0.8	5.4	-8.06	-53.1	0.704139	-1.4
BB6	Cilaos	30/11/2017	1332	6.5	22.8	2.41	3.15	4.35	0.07	13.52	0.36	0.1	1.32	0.07	b.d.l.	2	-7.47	-49.7	0.704129	-2
BB7	Cilaos	30/11/2017	652	6.9	19.8	1.12	0.84	2.85	0.03	4.51	1.16	0.1	0.8	0.08	b.d.l.	0.8	-7.58	-50.6		-14.2
BBLEU1	Cilaos	29/06/2017	524	7.7	18.6	0.91	0.63	2.77	0.03	6.13	0.09	0.05	0.46	0.05	1.0	3.9	-8.08	-53.4	0.704203	-6.1
BC	St-Benoît	15/12/2015	3270	6.5	23	4.08	13.31	7.86	0.45	42.98		0.12	2.1	0.10	b.d.l.	1.3	-7.62	-43.4	0.704196	-3.2
BE	Cilaos	26/10/2017	1257		19.8	2.17	4.3	1.83	0.15		0.03	0.1	1.77	0.06	b.d.l.	5.9	-8.15	-55.1	0.704167	-1.3
BR14	Cilaos	06/03/2016	1630	6.2	42.4	2.22	2.38	10.68	0.32	19.52**		0.68	2.35	0.95	0.2	11	-8.19	-51.9	0.704156	-1.5
BR14	Cilaos	21/11/2015	1684	6.1	39.1	2.65	2.69	12.03	0.33	21.97**		1.07	2.39	0.57	0.1	13.1	-8.44	-52.5	0.704172	-0.2
BR14*	Cilaos	08/09/2017	1764	6.8	37.2	2.17**	2.54	12.36	0.35	19.10**	0.91	1.21	2.49	0.97	b.d.l.	12.6	-8.53	-53.7	0.704179	-0.8
BR16*	Cilaos	30/07/2016	2530	6.8	25.9	2.52**	2.39	18.35	0.86	24.93**		3.22	2.02	2.70	b.d.l.	8	-8.41	-52	0.704165	1.8
BR16*	Cilaos	29/10/2017	3370	6.5	29.1	2.70**	3.14	25.01	0.99	31.61**	0.48	5.13	2.58	4.02	b.d.l.	11.1	-8.67	-53.3	0.704162	0.6
BR21*	Cilaos	23/08/2016	1256	6.2	25.1	1.64**	0.58	9.8	0.1	12.98**	0.5	0.36	0.56	0.38	b.d.l.	17.6	-8.07	-51.7	0.704249	3
BR6	Cilaos	26/08/2017	1221	6.1	25.3	3.42	1.15	2.93	0.09	10.16	0.44	0.1	0.93	0.09	b.d.l.	10.9	-7.35	-46	0.704212	-1.5
BR9	Cilaos	20/03/2016	1149	6.0	26.5	2.53	3.06	2.6	0.12	13.85**		0.05	1.64	0.05	b.d.l.	10.5	-7.96	-53.1	0.704175	0.1
DUP*	Salazie	15/06/2015	714	8.1	23.3	1.39	1.25	2.78	0.08	7.23	0.39	0.06	0.96		b.d.l.		-6.5	-38.4	0.704224	3.4
EDN*	Salazie	16/05/2015	1855	7.7	25.5	3.17	3.17	6.17	0.22	23	0.12	0.05	2.34		0.0		-6.5	-38.7	0.704237	3
FSJ2	Salazie	14/07/2017	864	7.1	15.8	2	1.25	2.35	0.07	8.70**	0.07	0.08	1.36	0.08	b.d.l.	7.8	-5.96	-34.4	0.704240	-2.6
G3	Cilaos	20/03/2016	1416	6.2	22.4	3.34	4.27	2.66	0.13	17.97**		0.05	2	0.13	b.d.l.	18.1	-8.23	-51.9	0.704183	0.2
GDS*	Salazie	17/06/2015	1234	7.7	18.7	4.74	2.23	1.31	0.07	8.79	3.34	0.03	0.79	0.14	0.0		-5.9	-33.1	0.704330	1.7
IRN*	Cilaos	29/11/2017	2570	6.7		4.00**	4.19	15.13	0.19	29.48**	1.04	0.15	2.51	0.10	b.d.l.	19.8	-8.14	-51.1		
IRN*	Cilaos	05/05/2017	2510	6.5	35.1	**	4.16	15.01	0.21		1.01	0.17	2.32	0.11	b.d.l.	12.2	-8.05	-51		-1.2
IRN*	Cilaos	15/06/2017	2500	6.4	36	3.99**		14.79	0.2	28.98**	1.01	0.15	2.36	0.17	b.d.l.	19.7	-8.1	-51.2		-0.9
IRN*	Cilaos	26/10/2017	2570	6.4	34.3	4.05**	4.26	15.33	0.2	29.92**	1.04	0.15	2.43	0.11	b.d.l.	20	-8.06	-51		-0.5
IRN*	Cilaos	25/09/2017	2560	6.6	36.2	4.00**	4.15	15.05	0.2	29.36**	1.02	0.16	2.42	0.10	b.d.l.	19.4	-7.89	-50.9	0.704168	-0.5
IRN*	Cilaos	30/08/2017	2560	6.4	36.2	4.08**	4.17	15.46	0.22	28.97	1.04	0.21	2.41		b.d.l.	20	-8.04	-50.9		-0.4
MAN*	Salazie	16/06/2015	1395	6.6	30.6	3.3	2.69	4.39	0.2	16.57	0.11	0.07	1.76		0.0		-7.2	-43.4	0.704277	1.6
MAN	Salazie	19/08/2016	1520	6.7	30.4	3.6	2.84	4.45	0.21	17.16**	0.14	0.11	1.53	0.08	b.d.l.	9.7	-7.19	-42.5	0.704273	1.2
MANa	Salazie	19/08/2016	274	6.2	14.9	0.42	0.51	0.61	0.14	2.51**	0.03	0.05	0.65	0.04	b.d.l.	0.6	-8.58	-54.8	0.704240	1.5
MANc	Salazie	19/08/2016	687	5.9	17.5	1.27	1.5	1.79	0.24	7.39**	0.06	0.06	1.12	0.06	b.d.l.	2.6	-8.54	-53.8	0.704258	5.2
MANES	Cilaos	29/11/2017	2310	6.5	29.6	3.75	3.99	13.14	0.19	26.77**	0.9	0.26	2.21	0.12	b.d.l.	17.7	-8	-51.3		-0.9
MANES	Cilaos	26/10/2017	2340	6.0	30.3	3.55	3.99	13.02	0.2	23.82**	0.9	0.16		0.09		18.1	-8.06	-51.4		-1.4
MANES	Cilaos	25/09/2017	2310	6.6	30.8	3.78	3.99	13.18	0.2	27.00**	0.89	0.15		0.08		18.1	-7.98	-51		-1.3
MANES	Cilaos	30/08/2017	2320	6.4	30.7	3.72	3.93	12.94	0.2	26.52**	0.88	0.16		0.08		17.6	-8.02	-51.4		-0.8
MANES*	Cilaos	15/06/2017	2310	6.4	29.8	3.72**	3.86	13.02	0.2	26.52**	0.86	0.16		0.16		17.7	-8.04	-51.5		-1.2
MANES	Cilaos	05/05/2017	2300	6.4	30.5	3.66	3.99	13.23	0.19	26.75**	0.9	0.18				17.3	-8.03	-51.3		0
MVP1	Salazie	12/05/2017	476	7.9	21	1.56	0.88	0.48	0.04	2.69	1.29	0.11	0.59	0.22	0.8	4	-5.84	-35.2	0.704330	-12.9
OLIVbis	Salazie	22/11/2017	551	8.1	22.3		0.87	1.62	0.04	5.05**	0.45	0.11	0.5	0.08	b.d.l.		-6.01	-37.1	0.704364	-12.3
OLIVbis	Salazie	30/01/2018	735	7.8	22.3	1.92	1.23	1.59	0.04	2.39**	1.37	0.13			b.d.l.	7.1			0.704347	-12.1
PEND	Cilaos	29/11/2017	618	7.1	22.9	0.89	0.98	2.86	0.14	5.41**	0.6	0.13	0.94	0.11	b.d.l.	0.5	-8.18	-58.8	0.704212	-14.8

10

Spring	Location	Date dd/mm/yyyy	Electrical Conductivity (µS/cm)	pH	Temperature (°C)	Ca (mmol/L)	Mg (mmol/L)	Na (mmol/L)	K (mmol/L)	HCO_3 (mmol/L)	SO_4 (mmol/L)	Cl (mmol/L)	SiO_2 (mmol/L)	Br (µmol/L)	Al (µmol/L)	Sr (µmol/L)	$\delta^{18}O$ (‰ VMOW)	δD (‰ VMOW)	$^{87}Sr/^{86}Sr$	$\delta^{13}C$ (‰ PDB)
RB1*	Salazie	15/10/2016	929	6.0	19.8	2.30**	1.83	1.21	0.19	9.44**	0.08	0.05	1.62	0.09	b.d.l.	4.5	-6.5	-37.1	0.704308	-1.9
RB2	Salazie	15/10/2016	1030	6.1	19.8	3.11	1.94	1.25	0.15	11.26**	0.1	0.05	1.53	0.08	b.d.l.	6.7	-6.37	-36.6	0.704309	-1.9
RBGR1	Cilaos	30/06/2017	1334	6.6	19	1.78	4.17	2.86	0.03	14.1**	0.3	0.09	1.63	0.04	b.d.l.	0.6	-6.9	-45.9	0.704176	-4.3
RBR3	Cilaos	23/08/2016	379	7.5	12.1	0.96	0.74	0.83	0.06	3.9	0.27	0.02	0.52	0.02	b.d.l.	3.6	-8.01	-50.4	0.704181	2.8
RBR5	Cilaos	23/08/2016	634	7.8	14	1.8	1.34	1.21	0.06	4.16	1.69	0.05	0.44	0.02	b.d.l.	11.6	-7.76	-48.1	0.704185	-0.2
RBR8	Cilaos	23/08/2016	1145	7.4	13.5	4.72	1.76	0.97	0.06	4.61	4.94	0.07	0.28	0.02	b.d.l.	21.9	-7.97	-50.2	0.704169	0.9
RM22	Salazie	17/05/2017	660	7.4	23.3	1.32	2.14	0.64	0.1	6.74	0.45	0.08	1.24	0.09	0.5	3	-5.98	-36.5	0.704216	-7.5
RR1*	Cilaos	30/07/2016	1586	6.2	32.5	2.29**	1.41	10.3	0.3	14.72**	0.91	1.47	1.77	1.25	b.d.l.	9.2	-8.48	-56.3	0.704167	2.6
TB*	Salazie	22/11/2017	1410	6.3	34.4	2.14**	1.03	9.35	0.29	14.08**	0.57	0.75	1.09	0.63	b.d.l.	7.6	-6.42	-38.7	0.704194	-1.7
TBA*	Salazie	15/06/2015	1718	6.3	26.6	4	2.46	7.07	0.16	16.95	0.97	0.1	2.08		0.0					
TBA	Salazie	11/05/2017	1651	7.0	26.4		2.5	6.96	0.16	14.74	1.85	0.11	2.07		b.d.l.		-6.59	-39.9	0.704265	0.3
TR*	Salazie	21/07/2017	379	7.3	20.8	0.71**	0.78	0.73	0.04	1.51**	1.08	0.07	0.54	0.11	0.9	1.9	-6.69	-41.1	0.704333	-8
TR*	Salazie	30/01/2018	1016	7.5	20.8		2.71	1.05	0.06		5.07	0.09	0.6		1.2				0.704308	-6.4
VERO	Cilaos	29/11/2017	1980	6.2	29.7	3.2	3.37	10.69	0.16	22.39**	0.74	0.14	2.03	0.10	b.d.l.	15.6	-7.97	-51.3		-2
VERO	Cilaos	26/10/2017	1994	6.1	29.5	3.13	3.47	10.93	0.16	21.74	0.74	0.12		0.10		15.4	-8	-51.5		-2.1
VERO	Cilaos	25/09/2017	1988	6.4	29.9	3.16	3.4	10.69	0.25	22.38**	0.72	0.25				15.3	-7.96	-51.4		-2.2
VERO*	Cilaos	15/06/2017	1938	6.2	29.5	3.16**	3.33	10.56	0.16	20.79	0.68	0.14		0.04		15.3	-7.96	-51.6		-2.2
VERO*	Cilaos	30/08/2017	1986	6.2	29.7	3.12**	3.36	10.65	0.16	22.21**	0.72	0.13		0.06		15.2	-7.96	-51.2		-2.2
VERO	Cilaos	05/05/2017	1888	6.4	29.3	3.01	3.16	10.21	0.18	19.52	0.67	0.14		0.05		14.7	-7.93	-51.3		-2.3

316 *Bénard et al., (2020) ; **corrected values (re-analyzed Ca concentrations and HCO_3 concentrations estimated from ionic balance)

11

317 Table 2: monitoring of δ^{18}O and δD values (‰ VSMOW) from rainwaters and thermal springs (TBA and IRN) in the
318 cirques of Salazie and Cilaos. Rainwater samples correspond to a cumulate of rainfalls collected over about 4 weeks.
319 Spring samples were taken when rainwaters were collected. Rainfall amount (mm) is deduced from the collected
320 rain volume, except when information is missing (no data or overflow indicated by an *). In the latter case, we
321 used the rainfall data from the closest METEOFRANCE meteorological station accessible at their online data
322 repository publitheque.meteo.fr (we accounted for a proportionality coefficient to adjust for the systematic
323 difference between METEOFRANCE and our rainfall data).

Location	Sampling period (Rain)/ Sampling date (Spring, end of period) Dates in dd/mm/yy	Rain				Spring (TBA in Salazie, IRN in Cilaos)	
		$\delta^{18}O$ (‰)	δD (‰)	Volume (L)	Rainfall (mm) corrected	$\delta^{18}O$ (‰)	δD (‰)
Salazie	07/04/17-11/05/17	-4.06	-16.8	5.2	67.5	-6.59	-39.9
	11/05/17-14/06/17	-3.11	-9.8	1.6	20.0	-6.72	-40.4
	14/06/17-21/07/17	-2.70	-5.2	0.7	9.0	-6.79	-40.3
	21/07/17-25/08/17	-2.07	1.8	1.2	14.9	-6.83	-40.0
	25/08/17-21/09/17	-3.77	-15.7	0.9	11.0	-6.92	-41.1
	21/09/17-19/10/17	-1.86	1.5	1.0	13.4	-6.97	-40.7
	19/10/17-22/11/17	-2.89	-8.7	2.6	34.1	-6.97	-40.8
	22/11/17-20/12/17	-1.49	3.2	0.0*	8.6	-7.05	-40.5
	20/12/17-30/01/18	-7.22	-47.3	20.0*	298.4	-6.53	-39.0
	30/01/18-31/05/18	-6.90	-42.8	20.0*	506.2	-6.60	-39.7
	31/05/18-17/07/18	-2.47	-1.3	2.0	25.8	-6.74	-39.6
	17/07/18-18/10/18	-2.24	-1.8	2.9	36.8	-6.88	-40.5
	18/10/18-07/11/18	-2.58	-10.0	1.4	18.1	-6.96	-40.1
	08/11/18-21/01/19	-5.61	-32.3	11.1	143.3	-6.81	-40.3
	21/01/19-12/02/19	-5.19	-29.0	1.6	20.7	-6.83	-40.5
	12/02/19-13/03/19	-3.61	-15.5	1.9	23.9	-6.89	-40.3
	13/03/19-17/04/19	-4.73	-25.3	2.4	31.0	-6.96	-40.4
	17/04/19-28/05/19	-2.66	-4.4	1.5	19.4	-7.03	-40.5
Cilaos	30/03/17-05/05/17	-4.40	-18.4	0.0*	53.7	-8.05	-51.0
	05/05/17-15/06/17	-3.61	-18.2	1.0	12.3	-8.10	-51.2
	15/06/17-28/07/17	-2.67	-4.6	0.7	9.0	-8.09	-51.2
	28/07/17-30/08/17	-2.70	-5.1	1.0	12.9	-8.04	-50.9
	30/08/17-25/09/17	-2.76	-2.8	0.8	9.7	-7.89	-50.9
	25/09/17-26/10/17	-1.31	4.4	0.3	3.2	-8.06	-51.0
	26/10/17-29/11/17	-3.16	-11.7	1.8	23.6	-8.14	-51.1
	29/11/17-21/12/17	-2.74	-7.2	0*	10.1	-8.09	-51.3
	21/12/17-06/02/18	-8.34	-57.8	20.0*	304.4	-8.05	-51.5
	06/02/18-21/05/18	-9.68	-66.3	20.0*	430.9	-8.10	-51.6
	21/05/18-15/10/18	-2.25	-1.9	2.6	32.9	-8.10	-50.9
	15/10/18-08/11/18	-4.97	-25.3	2.2	27.8	-8.11	-51.1
	08/11/18-05/12/18	-3.70	-17.3	2.0	25.2	-8.13	-51.4
	05/12/18-22/01/19	-5.69	-34.8	3.9	50.4	-8.12	-51.6
	22/01/19-13/02/19	-5.20	-25.8	2.0	25.8	-8.11	-51.2
	13/02/19-14/03/19	-3.59	-15.8	0.9	11.6	-8.11	-51.2
	14/03/19-18/04/19	-4.86	-26.6	1.6	20.7	-8.12	-50.8
	18/04/19-29/05/19	-3.24	-8.3	0.6	7.1	-8.17	-50.9

324   Table 3: $^{87}Sr/^{86}Sr$ isotopic ratios of rocks from the cirques of Salazie and Cilaos.

Sample	Rock type	Source of data	Location	X (RGR92 /UTM40S)	Y (RGR92 /UTM40S)	Sr (ppm)	$^{87}Sr/^{86}Sr$	Error (2σ)	Stage
BR14	Syenite	This study	Cilaos			40.0	0.704184	0.000006	Differentiated
CHAP	Syenite		Cilaos			149	0.704215	0.000023	Differentiated
RN18-5	Syenite		Salazie			634	0.704182	0.000015	Differentiated
BAF1-6	Trachyte		Summit			498	0.704156	0.000010	Differentiated
PdNMS21	Aphyric Basalt	Smietana, 2011	Cilaos	340237	7648804	393.8	0.704153	0.000004	Shield
PdNMS21	Aphyric Basalt		Cilaos	340237	7648804	289.2	0.704153	0.000004	Shield
CB16290513	Gabbro	Berthod, 2016	Salazie	343698	7670796		0.704220	0.000010	Shield
CB2150914	Gabbro		Salazie	343808	7669712	54.8	0.704166	0.000009	Shield
CB2260513	Gabbro		Salazie	344106	7670815	288.4	0.704258	0.000007	Shield
CB3230914	Syenite		Salazie	343534	7670756	331.6	0.704190	0.000008	Differentiated
CB3A260513	Gabbro		Salazie	344120	7670828	245.7	0.704255	0.000010	Shield
SAB 1	Syenite	Nauret et al., 2019	Salazie	341515	7669423	245.0	0.704155	0.000008	Differentiated
SAL 1	Basalt		Salazie	344105	7670824	542.6	0.704283	0.000022	Shield
SAL 102	Oceanite		Salazie	344238	7670893	497.5	0.704041	0.000008	Shield
SAL 106	Gabbro		Salazie	344194	7670885	558.5	0.704290	0.000008	Shield
SAL 110	Gabbro		Salazie	343667	7670778	472.5	0.704256	0.000008	Shield
SAL 153	Oceanite		Salazie	342913	7674274	228.9	0.704085	0.000007	Shield
SAL 18	Gabbro		Salazie	344180	7670872	512.7	0.704290	0.000012	Shield
SAL 200	Trachy-Basalt		Salazie	343775	7669845	573.9	0.704158	0.000007	Differentiated
SAL 200 (duplicate)	Trachy-Basalt		Salazie	343775	7669845		0.704159	0.000007	Differentiated
SAL 201	Trachy-Basalt		Salazie	343895	7669717	376.8	0.704268	0.000006	Differentiated
SAL 203	Trachy-Basalt		Salazie	343317	7670409	487.4	0.704167	0.000007	Differentiated
SAL 206	Dunite		Salazie	344492	7668744	23.9	0.704277	0.000011	Shield
SAL 48	Basalt		Salazie	343567	7670290	512.4	0.704223	0.000008	Shield
SAL 51	Basalt		Salazie	343482	7670368	357.1	0.704223	0.000010	Shield
SAL 88	Trachyte		Salazie	344734	7670476	531.1	0.704169	0.000008	Differentiated
SAL 88 (duplicate)	Trachyte		Salazie	344734	7670476		0.704185	0.000009	Differentiated
RUN 027-2006	Olivine basalt		Cilaos			89.0	0.704154	0.000008	Shield
RUN 029-2006	Olivine basalt		Cilaos			73.5	0.704144	0.000010	Shield
RUN 040-2006	Benmoreite		Salazie			89.0	0.704504	0.000015	Differentiated
ANTN	Benmoreite		Summit			176	0.704176	0.000014	Differentiated
RN18-9	Trachyte		Summit			256	0.704153	0.000010	Differentiated

325

4.   Discussion

### 4.1. Spatial distribution of hydrothermal features

328   In this section, we study the spatial distribution of several geochemical features related to
329   hydrothermal activity: the occurrence of field indicators of hydrothermal activity, the temperature and
330   electrical conductivity at the outlets of springs and their CO_2 partial pressure. This spatial distribution
331   is then superimposed to the main geological features to decipher if they may constitute heat sources
332   or drains for the thermal fluids.

4.1.1.   Field indicators of hydrothermal activity

334   Thermal springs and dry deposits of iron oxide/carbonate/sulfide, which are indicators of
335   hydrothermal activity, are observed in the three cirques (Figure 3) with two springs reaching farther
336   east in Saint-Benoît. The majority of them are found in the cirques of Salazie and Cilaos, with a greater

13

337 abundance in the upper slopes of the cirques beneath the summit of Piton des Neiges. A first important
338 result of our field prospection is that hydrothermal indicators largely extend outside the proposed
339 caldera, suggesting that the hydrothermal system is not directly fed by this major volcanic structure
340 nor limited by it. Secondly, most of these indicators are spread along a ~N25° axis, coinciding with the
341 N30° rift zone defined by Chaput et al., (2017, 2014). This N25° spatial repartition is not biased by
342 prospecting, as rivers from the northeastern part of Salazie, from the western part of Cilaos, from
343 Mafate, from the two branches of the Grand Bassin depression, and from the Marsouins basin were
344 surveyed and found to be devoid of thermal springs. Based on a study of outcropping planar intrusions,
345 Chaput et al., (2017) showed that the N30°E rift zone is composed of mafic and differentiated dykes,
346 implying a more recent activity than the N110-160° rift zone composed only of mafic intrusions. Our
347 study confirms that the N30° rift zone is the most recently active volcano-tectonic lineament in the
348 edifice, sufficiently young to provide heat for a shallow hydrothermal system. Thirdly, dry deposits
349 (sulfides, oxides or carbonates) are mostly found at the external parts of the area containing
350 hydrothermal indicators, and principally at the northern and southern extremities of this ~N25°-
351 elongated zone. This suggests that dry hydrothermal indicators correspond to the external limits of the
352 hydrothermal system. Interestingly, the two boreholes drilled in Salazie are located in this zone of dry
353 hydrothermal indicators, possibly outside the hydrothermal system, which may explain why these two
354 boreholes found heat but no water yield.

355
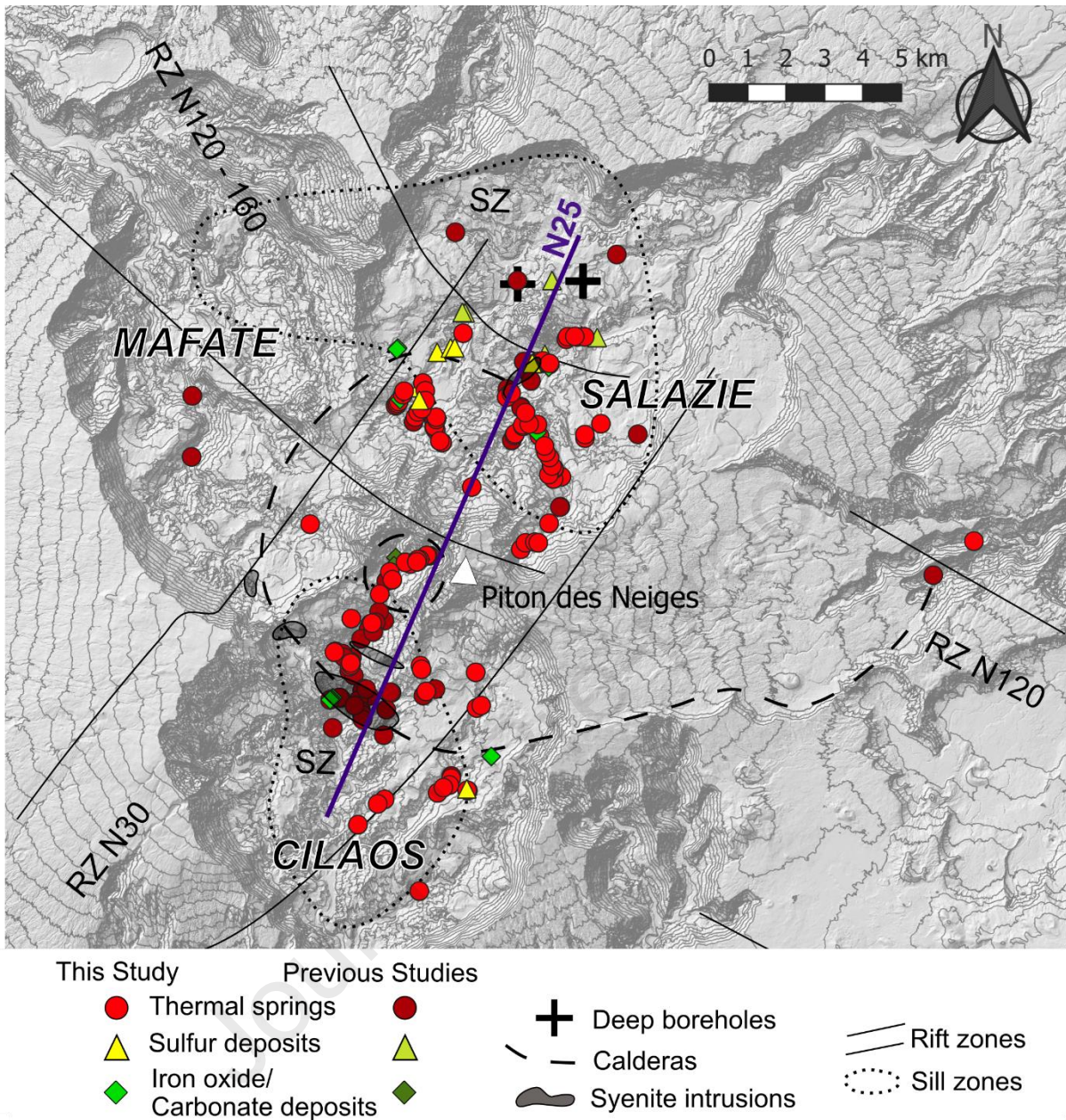
Figure 3: Map of the field indicators of hydrothermal activity at Piton des Neiges volcano from this study (bright shades) and previous studies (darker shades, Aunay et al., 2013; Belle, 2014; Frissant et al., 2003; Iundt et al., 1992; Lopoukhine and Stieltjes, 1978; Louvat and Allègre, 1997; Sanjuan et al., 2001). These indicators include thermal springs and sulfur, iron oxide, or carbonate dry deposits. Most of the indicators are spread along a ~N25° axis, coinciding with the N30° rift zone.

361   *4.1.2. Temperature and electrical conductivity*

High temperatures and elevated amounts of total dissolved solids (proxied by EC) at the outlet of thermal springs are indicators of hydrothermal activity. These physicochemical parameters can be modified during fluid upflow from the geothermal reservoir to the surface by mixing with shallow cold waters, by further interaction with the surrounding rocks, or by cooling and deposition of secondary minerals. Thermal springs display various degrees of enrichment in dissolved solids and warming compared to rivers and groundwaters of Salazie and Cilaos (Figure 4), reflecting varying contributions of a hydrothermal component. Those displaying higher values for outlet temperature and/or EC indicate a closer reservoir, a faster transfer from the reservoir to the surface, a higher intensity of

15

370   water/rock interaction, or a lower dilution by cold waters. These physicochemical parameters are thus
371   of paramount importance in geothermal exploration to locate zones of fastest circulation and/or of
372   highest fluid temperature. The thermal springs of Piton des Neiges are represented according to their
373   outlet temperature and EC in Figure 5. This figure shows that the hottest and most mineralized springs
374   are not only located along the N30°E rift zone, but also in immediate vicinity of syenite intrusions
375   and/or along the proposed rim of the caldera. Previous work suggested that syenite intrusions, thought
376   to delineate the caldera, play at least a role of drain transferring thermal waters from the reservoir to
377   the surface, and possibly even constitute the heat source and/or the reservoir itself (e.g. Frissant et
378   al., 2003; Sanjuan et al., 2001). Our study strengthens these conclusions, as they remain valid even
379   with our larger dataset.
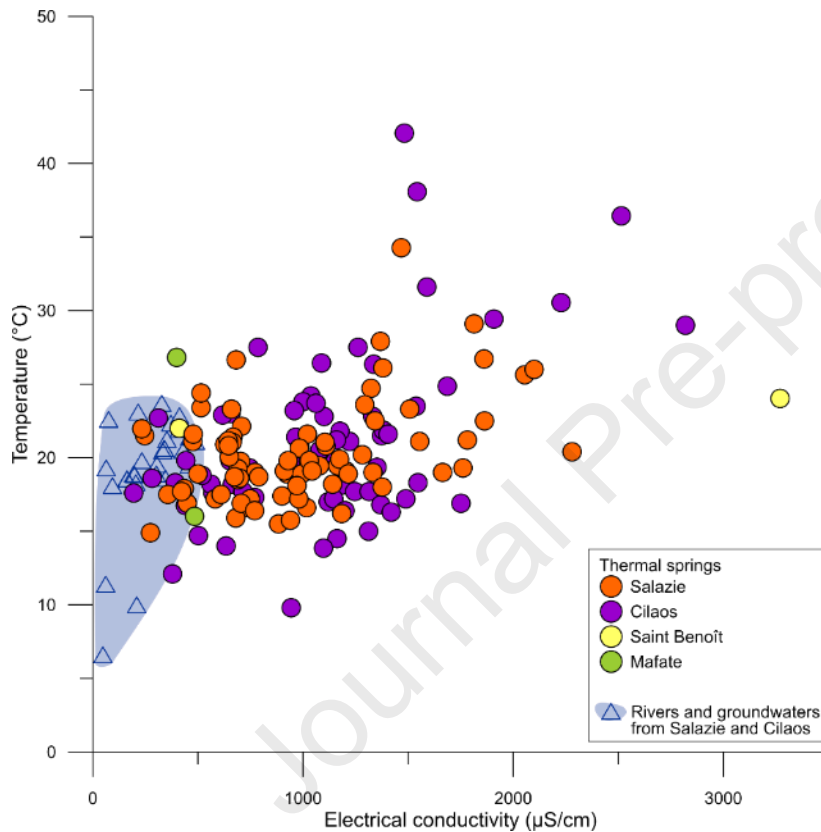
380

381   Figure 4: Mean temperature (°C) and electrical conductivities (µS/cm) of thermal springs from Piton de Neiges (this
382   study, Aunay et al., 2013; Belle, 2014; Frissant et al., 2003; Iundt et al., 1992; Lopoukhine and Stieltjes, 1978;

16

383 Louvat and Allègre, 1997; Marty et al., 1993; Poul, 1966; Sanjuan et al., 2001) and rivers and groundwaters of
384 Salazie and Cilaos (this study, Belle, 2014; Louvat and Allègre, 1997).
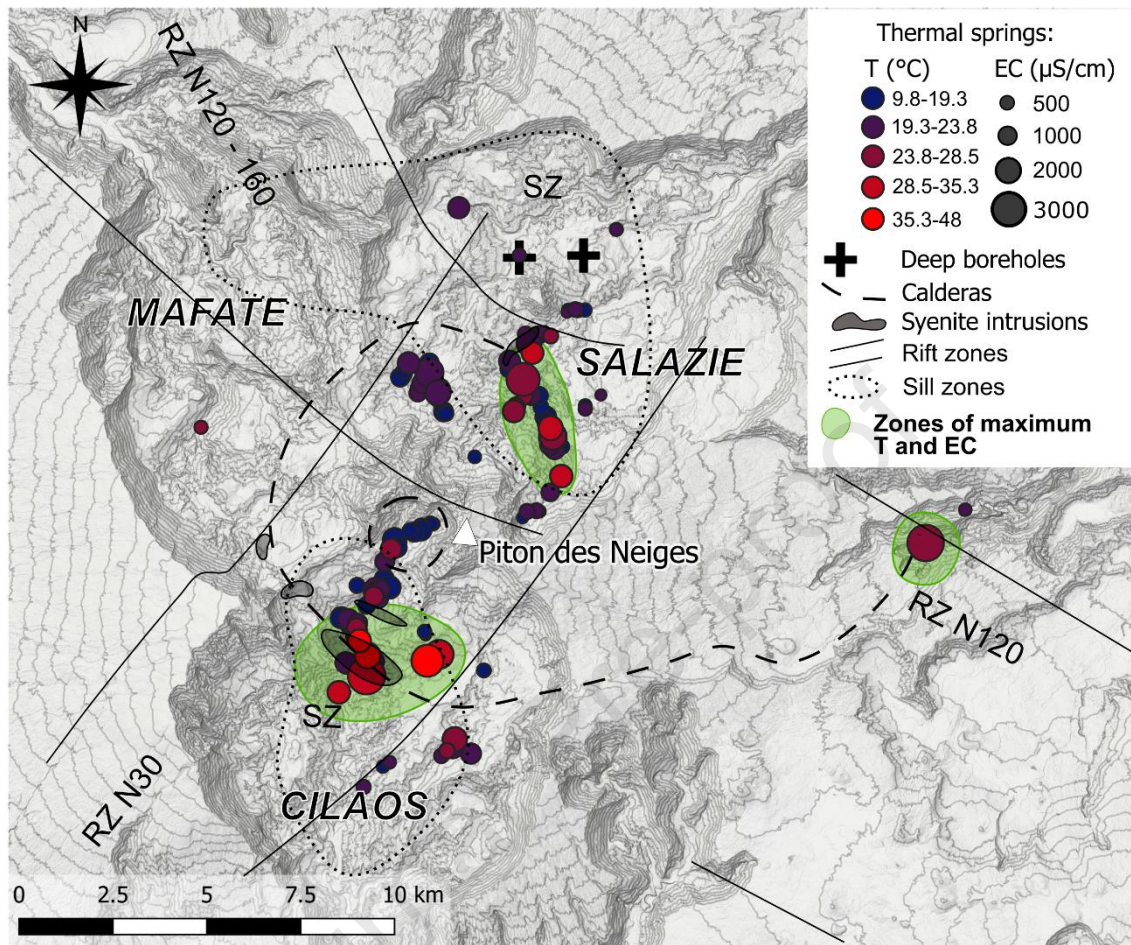

385

386 Figure 5: Spatial distribution of temperature (represented by a color scale) and electrical conductivity (EC in µS/cm,
387 represented by symbol size) in the thermal springs of Piton des Neiges. Green fields represent zones of highest
388 temperatures and EC, and hence of most promising geothermal resource according to these parameters. Volcano-
389 tectonic structures (rift zones, sill zones, syenite intrusions, and calderas) are also represented.

390   *4.1.3.   Magmatic CO₂*

391 All the thermal springs of Piton des Neiges analyzed in previous studies display evidence of interaction
392 with magmatic CO_2, which essentially comes from mantle degassing associated with the Réunion
393 hotspot (Bénard et al., 2020). The $\delta^{13}C$ signature of this mantellic CO_2 has been estimated from gas
394 and fumarole samples of Piton de la Fournaise, the active volcano of La Réunion, and is comprised
395 between -0.5 and -8 ‰ (Boudoire et al., 2018; Marty et al., 1993; Trull et al., 1993). Bénard et al.,
396 (2020) showed that higher values may be measured in thermal springs due to loss of gaseous CO_2 from
397 waters which results in isotopic fractionation. Lower values may also be expected due to mixing with
398 a biogenic carbon source with $\delta^{13}C \leq -20$ ‰ (Liuzzo et al., 2015). The newly measured values of $\delta^{13}C$ in
399 thermal springs (from -14.8 to 5.15 ‰) from this study are consistent with the previous observations.
400 Only four springs (BB7, MVP1, OLIVbis, PEND) display $\delta^{13}C$ values lower than -8 ‰, indicating a slight
401 biogenic contribution. Therefore, magma degassing is the main carbon source in thermal springs and
402 consequently, CO_2 can be used to highlight magmatic processes.

17

403   Consequently, we use the spatial distribution of the carbon content to locate zones of maximum CO_2
404   degassing, which may be interpreted as preferential pathways in the edifice for the rise of deep fluids.
405   For each thermal spring, we computed the mean partial pressure of CO_2 (PCO_2, Table 4) at the outlet,
406   from the water compositions displayed in Table 1 and using the "Diagrammes" software (created by
407   R. Simler, Université d'Avignon et pays du Vaucluse, http://www.lha.univ-avignon.fr/LHA-
408   Logiciels.htm) from PhreeqC, USGS®, with the WATEQ4F thermodynamic database (Ball and
409   Nordstrom, 1991). Most of the gas being already lost at the spring outlet (Bénard et al., 2020; Marty
410   et al., 1993; Sanjuan et al., 2001), PCO_2 cannot be considered as entirely representative of the total
411   carbonate species' concentrations at depth. However, the preservation of a high PCO_2 in thermal
412   springs is an indicator of an initial elevated CO_2 input and/or a shorter pathway from depth to surface.
413   In Figure 6, we displayed the spatial distribution of PCO_2 along with geological features. It is worth
414   noting that the thermal springs with the highest PCO_2 are not necessarily those with a high outlet
415   temperature or EC, showing that CO_2 input is disconnected from the heat source. Nevertheless, as for
416   temperature and EC, the most enriched springs ($PCO_2 > 500$ mbar) are those located in the N30°E rift
417   zone and in the vicinity of syenite intrusions and/or along the proposed rim of the caldera, except for
418   spring BC. The thermal spring BC, also displaying a high PCO_2, is located west of these structures, on
419   the rift zone N120°E running throughout the island between Piton de la Fournaise and Piton des
420   Neiges. CO_2 anomalies in soils have been observed along this rift zone (Boudoire et al., 2017). This
421   spatial repartition suggests that the N30°E and N120°E rift zones and syenite intrusions and the larger
422   caldera represent preferential pathways for the rise of CO_2 into the hydrothermal system.
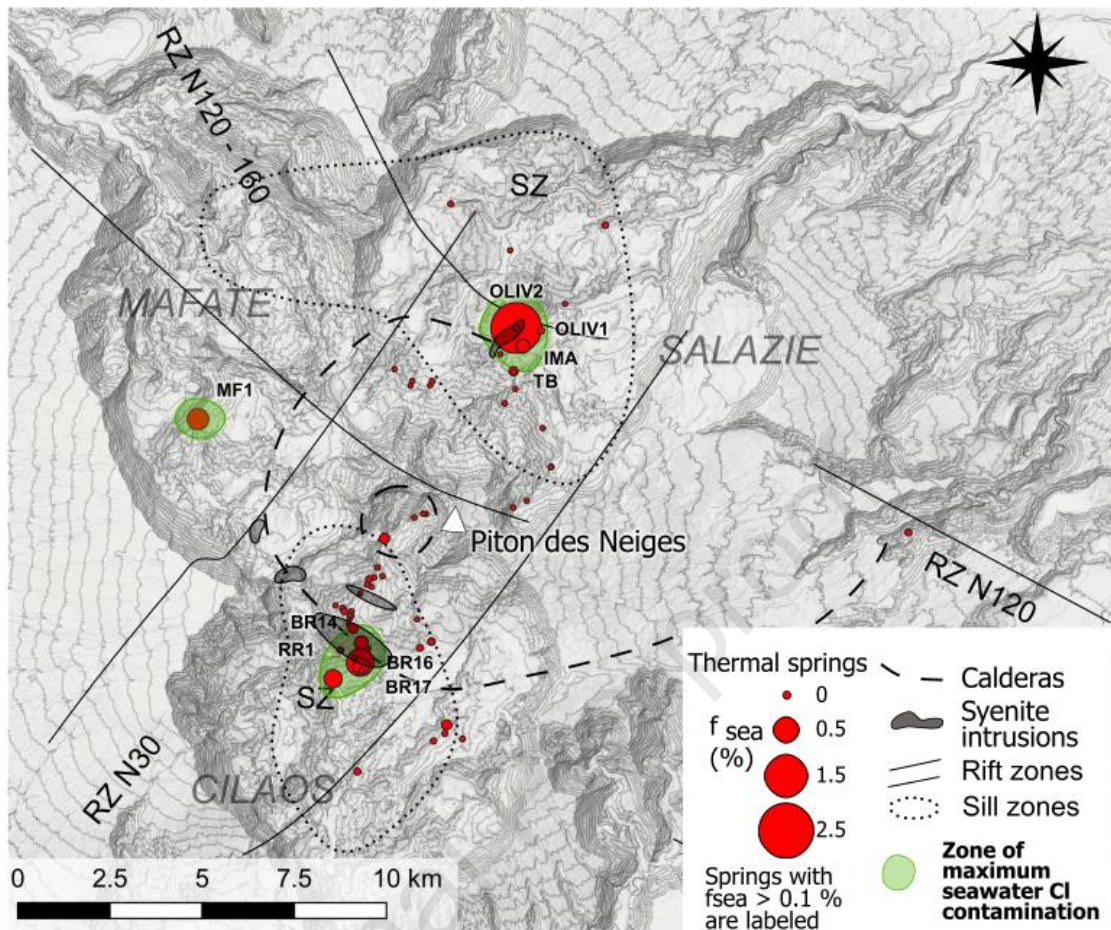
18

423
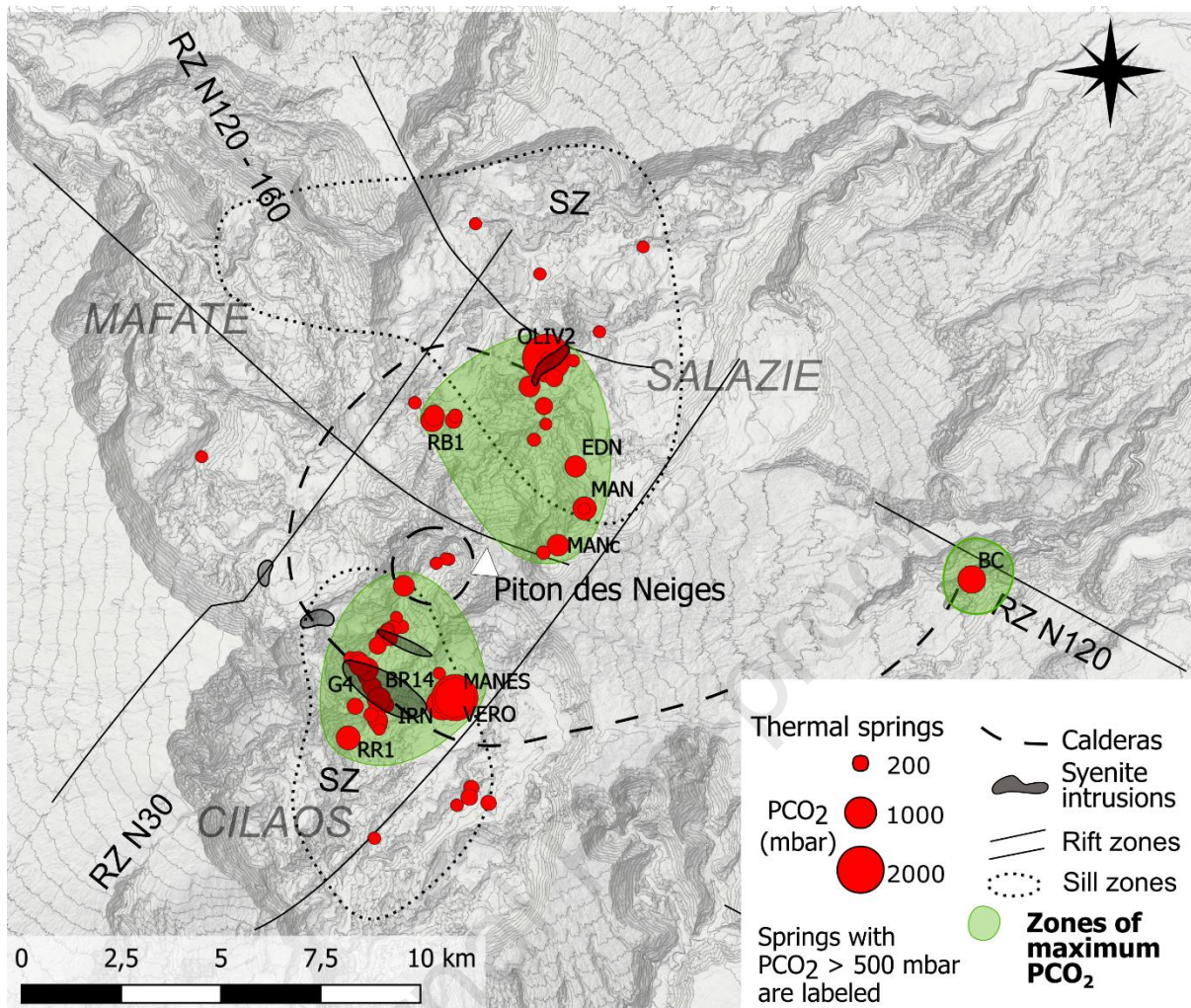
Figure 6: Spatial distribution of the mean partial pressure of CO_2 (PCO_2, in mbar) at the outlet of thermal springs from Piton des Neiges, relative to volcano-tectonic structures (rift zones, sill zones, syenite intrusions, calderas). Green fields represent zones of higher PCO_2, which are interpreted as zones of preferential mantle degassing. Volcano-tectonic structures (rift zones, sill zones, syenite intrusions, and calderas) are also represented.

4.2. Hydrogeological features

4.2.1. Contamination by elements originating from seawater

From the study of the $\delta^{37}Cl$ signature of thermal springs, Bénard et al., (2020) showed that two main end-members contribute to their Cl budget: seawater and freshwater recharge. This is confirmed by the Cl/Br concentration ratios obtained from this study which correspond to that of seawater (Figure 7). This seawater contamination likely does not originate from a current connection to the sea, as saltwater intrusion is limited to coastal areas in La Réunion (Dumont et al., 2018). It could however come from a trapped ancient reservoir or from seawater residual brines from when the area was still connected to the sea, as observed in other volcanic islands (Herrera and Custodio, 2014). Whatever its origin, this seawater Cl source is located at a depth of at least that of the seawater table.

19

Figure 7: Cl and Br molar concentrations of the thermal springs of Piton des Neiges (This study, Sanjuan et al., 2001) compared to the seawater dilution line.

In this section, we quantify the contamination by seawater Cl in thermal springs and use its spatial distribution to locate the seawater Cl source in connection with the hydrothermal system. For each thermal spring, we calculated the molar proportion of seawater contamination in thermal springs (f_{sea}, in mol%) using Cl as a conservative tracer, as shown in equation 1 (Appelo and Postma, 2005):

$$f_{sea} = \frac{m_{sample} - m_{fresh}}{m_{sea} - m_{fresh}} \quad (1)$$

where m_{sample}, m_{sea}, and m_{fresh} represent the Cl molar concentrations of the sampled thermal spring, of seawater and of freshwater recharge, respectively. For each spring, m_{sample} is calculated as the median composition of all available Cl analyses from this study and previous studies. We use the mean Cl concentration of seawater for m_{sea}. For freshwater recharge, we considered a representative set of 131 analyses of groundwaters and river waters from Réunion Island (Aunay et al., 2012; Aunay and Gourcy, 2007; Belle, 2014; Frissant et al., 2005; Louvat and Allègre, 1997; Petit et al., 2013) as background values. We used the median Cl concentration of this dataset for m_{fresh}. There is very little seawater contamination in the thermal springs of Piton des Neiges. Out of the 70 thermal springs for which Cl concentrations are available, 61 contain less than 0.1 mol% seawater (Table 4). The highest proportion of seawater is found in OLIV2 spring, reaching 2.34 mol%. The hydrothermal system is thus located above the top of the seawater table, except for a limited number of springs whose drain may root deep enough to intersect a seawater, Cl-rich reservoir. Seawater Cl contamination is found in the vicinity of syenite intrusions and along the rim of the caldera, as are the hottest and most mineralized thermal springs (Figure 8). This suggests that these structures represent pathways for the deepest geothermal fluids reaching the surface.

20

461

Figure 8: Spatial distribution of seawater contamination (in mol%) in the thermal springs of Piton des Neiges relative
to volcano-tectonic structures (rift zones, sill zones, syenite intrusions, and calderas). Green fields represent zones
of highest seawater contamination, interpreted as the deepest drains for the ascent of hydrothermal fluids. Volcano-
tectonic structures (rift zones, sill zones, syenite intrusions, and calderas) are also represented.

466

21

467 Table 4: Mean values of partial pressure of CO_2 at spring outlet (PCO_2, in mbar), molar proportion of seawater
468 contamination (f_{sea}, in mol%), $\delta^{18}O$ and δD (in ‰ VSMOW) for each thermal spring.

Thermal spring	Mean PCO$_2$ (mbar)	Mean f$_{sea}$ (mol%)	Mean δ^{18}O (‰)	Mean δD (‰)	Thermal spring	Mean PCO$_2$ (mbar)	Mean f$_{sea}$ (mol%)	Mean δ^{18}O (‰)	Mean δD (‰)
AGS	237	0.00			G2	101	0.00		
BACH	70	0.00	-6.70	-39.4	G3	381	0.00	-8.23	-51.9
BB	162	0.05	-8.13	-53.7	G4	537	0.00		
BB6	249	0.00	-7.47	-49.7	GDS	95	0.18	-5.40	-28.3
BB7	33	0.00	-7.58	-50.6	IMA	259	0.01		
BBLEU1	7	0.00	-8.08	-53.4	IRN	1075	0.00	-8.07	-51.1
BC	865	0.01	-7.62	-43.4	MAN	628	0.00	-7.24	-43.6
BE	213	0.00	-8.15	-55.1	MAN G	12	0.00	-7.00	-39.8
BR1	97	0.00			MANa	90	0.00	-8.58	-54.8
BR10	387	0.00			MANc	530	0.01	-8.54	-53.8
BR11	16	0.00			MANES	1900	0.39	-8.04	-51.7
BR12	382	0.04	-8.20	-50.5	MF1	0	0.00		
BR13	6	0.00			MVP1	2	0.23	-5.84	-35.2
BR14	641	0.13	-8.33	-52.5	OLIV1	28	2.34	-6.50	-40.1
BR15	72	0.01			OLIV2	2583	0.00	-7.80	-45.9
BR16	440	0.68	-8.54	-52.7	OLIVbis	4	0.00	-6.01	-37.1
BR17	273	0.21			PC	17	0.01		
BR18	3	0.00			PEND	23	0.00	-8.18	-58.8
BR2	4	0.00			PISSA	154	0.00	-6.70	-41.4
BR21	487	0.05	-8.07	-51.7	RB1	588	0.00	-6.50	-37.1
BR27	265	0.01			RB2	484	0.00	-6.37	-36.6
BR3	220	0.00			RBGR1	174	0.00	-6.90	-45.9
BR4	120	0.00			RBR3	6	0.00	-8.01	-50.4
BR5	66	0.01			RBR5	4	0.00	-7.76	-48.1
BR6	404	0.00	-7.35	-46.0	RBR8	8	0.00	-7.97	-50.2
BR7	279	0.00			RFOUQ	496	0.00	-6.50	-37.9
BR8	67	0.00			RM22	16	0.25	-5.98	-36.5
BR9	603	0.00	-7.96	-53.1	RR1	656	0.01	-8.48	-56.3
DUP	3	0.00	-6.50	-38.4	sRMAT	14	0.00	-5.90	-36.5
EDN	517	0.00	-6.50	-38.7	sRMAT2	46	0.04	-6.20	-35.5
FJ1	93	0.00			sRMAT3	43	0.12		
FJ2	224	0.00			TB	305	0.00	-6.42	-38.7
FJ3	106	0.00			TBA	291	0.00	-6.83	-40.5
FSJ2	35	0.00	-5.96	-34.4	TR	7	0.01	-6.50	-40.7
G1	108	0.00			VERO	1530		-7.98	-51.4

469

4.2.2. Recharge

471 Mean values of $\delta^{18}O$ and δD for each thermal spring computed from our new and previous data (Table
472 4) plot close to the local meteoric water line (Figure 9.A). This $\delta^{18}O$ and δD signature indicates that the
473 hydrothermal system is supplied by rain infiltration, as already evidenced by Bénard et al., (2020). With
474 our new data, however, $\delta^{18}O$ and δD reveal a dichotomy between the thermal springs of Salazie and
475 Cilaos. $\delta^{18}O$ and δD are less negative in the cirque of Salazie (from -7.80 to -4.9 ‰ and from -45.9 to -
476 23.5 ‰, respectively) than in Cilaos (from -8.67 to -6.70 ‰ and from -58.8 to -41.4 ‰, respectively),
477 except for the two springs at the extreme south of the cirque of Salazie MANa (-8.6 and -54.8 ‰) and
478 MANc (-8.5 and -53.8 ‰, respectively) that show very negative values compatible with the Cilaos
479 group.

22

480
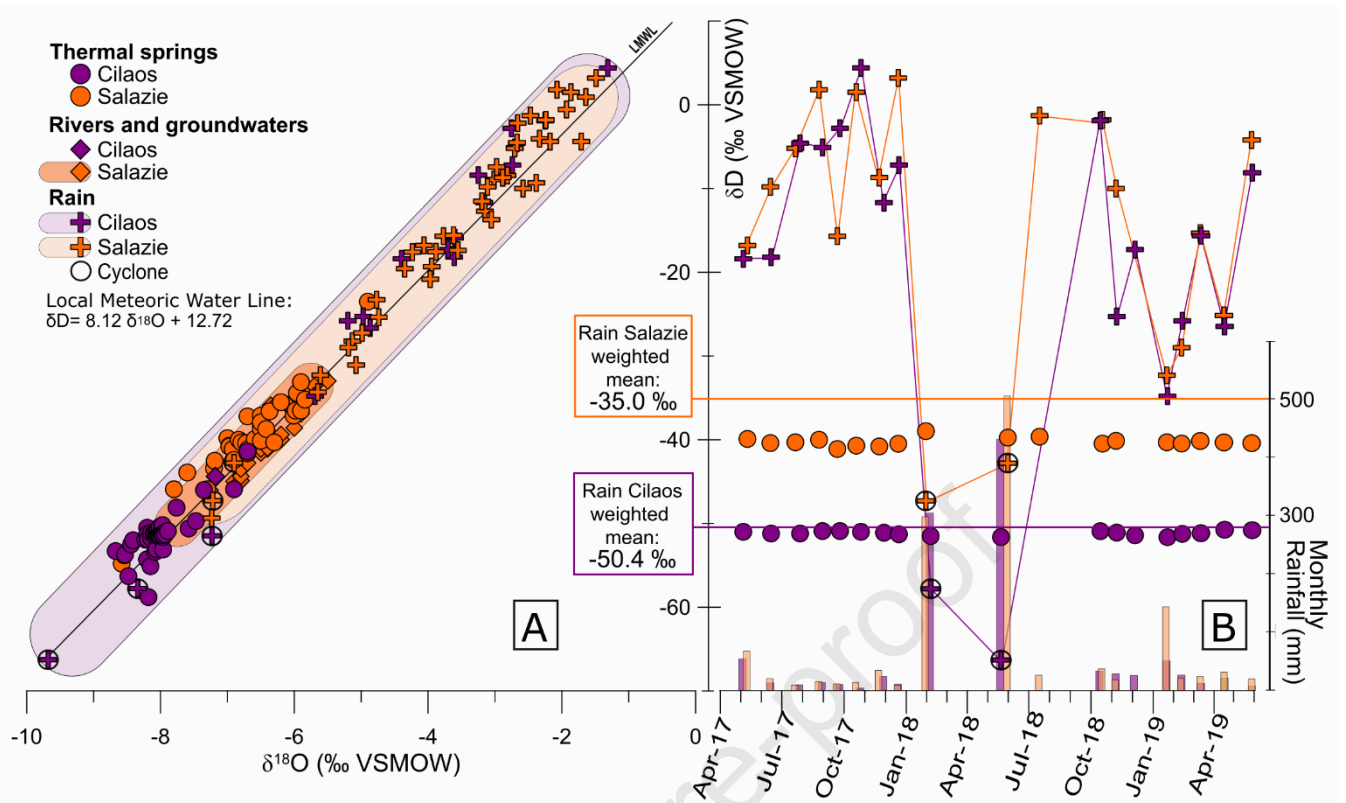
Figure 9: A. Mean $\delta^{18}O$ and δD isotopic ratios of thermal springs (this study, Aunay et al., 2013; Belle, 2014; Sanjuan et al., 2001) compared to that of river waters, groundwaters (this study, Belle, 2014; Louvat and Allègre, 1997) and rainwaters (this study, Belle, 2014; Grunberger, 1989; IAEA/WMO, 2019) from Salazie and Cilaos. Rainwaters from cyclones are circled in black. B. Comparative monitoring of the δD isotopic ratios (‰ VSMOW) of thermal springs and rain in Salazie and Cilaos, relative to rainfall heights (mm).

486 In order to understand this difference, we compared the $\delta^{18}O$ and δD values of thermal springs to that
487 of rivers, groundwater and rain in both cirques (Figure 9.A) and monitored $\delta^{18}O$ and δD for two years
488 in thermal springs IRN in Cilaos and TBA in Salazie and in rainfall at both sites (Figure 9.B). In Salazie,
489 the distribution of $\delta^{18}O$ and δD values of thermal springs is very similar to that of rivers and
490 groundwaters ($\delta^{18}O$ from -8.0 to -5.5 ‰ and δD from -46.1 to -33.0 ‰), indicating a similar recharge.
491 In Cilaos, the only river sample available (rBRO, from this study) displays $\delta^{18}O$ and δD values (-7.18 and
492 -44.4 ‰, respectively) in the range of that of thermal springs from Salazie and Cilaos, and that of rivers
493 and groundwaters from Salazie. Additional data would thus be necessary to discuss $\delta^{18}O$ and δD values
494 of rivers and groundwaters compared to thermal springs in the cirque of Cilaos. The range of $\delta^{18}O$ and
495 δD isotopic ratios in rains is similar in Salazie and Cilaos expect for 2 data points with lower values in
496 Cilaos corresponding to samples from cyclones (Figure 9).

497 We considered recharge by computing the volume-weighted mean $\delta^{18}O$ and δD isotopic ratios of rains
498 over two years for each cirque (2017-2019), using our monthly monitoring data at both sites (Table 2).
499 The weighted mean $\delta^{18}O$ and δD isotopic ratios in rainwater is much higher in the cirque of Salazie
500 ($\delta^{18}O$=-5.94 ‰ and δD=-35 ‰, Figure 9) than in Cilaos ($\delta^{18}O$=-7.70 ‰ and δD=-50.4 ‰). A similar
501 difference is also observed in the chronicles of rain analyses over the period 1985-1986 between
502 Salazie ($\delta^{18}O$=-6.50 ‰ and δD=-37.6 ‰) and Cilaos (weighted mean $\delta^{18}O$=-7.23 ‰ and δD =-51.5 ‰,
503 Grunberger, 1989). This difference is mostly visible during cyclones (Figure 9.B), which appear to
504 constitute a low $\delta^{18}O$ and δD end-member with different values for Salazie and Cilaos. The $\delta^{18}O$ and
505 δD dichotomy in thermal springs may thus be explained by a difference in the isotopic signature of the
506 recharge by cyclones between the two cirques. We tentatively explain this contrast by the isotopic air

23

507 masses distillation at their passage over Piton des Neiges summit, from the windward slopes in Salazie
508 to the leeward slopes in Cilaos. This strongly suggests that the Salazie and Cilaos hydrothermal
509 reservoirs are not connected.

510 In comparison with rains, the two monitored thermal springs display very limited temporal $\delta^{18}O$ and
511 δD variations (Figure 9.B). The Cilaos spring (IRN) is not only very stable (from -50.9 to -51.2 ‰, mean
512 -51.0 ‰ for δD), but also very close to the volume-weighted mean $\delta^{18}O$ and δD isotopic ratios of rains
513 in this cirque (-50.4 ‰ for δD, Figure 9.B). This stability holds over a ~20 year period with a δD value
514 of -51.3 ‰ measured at IRN in 2000 by Sanjuan et al., (2001). $\delta^{18}O$ and δD values of the Salazie thermal
515 spring (TBA) are also very stable over the two-year period (e.g. from -38.7 to -41.1 ‰, mean -40.2 ‰
516 for δD), and their mean is relatively close to the volume-weighted mean $\delta^{18}O$ and δD isotopic ratios of
517 rains in this cirque (-35 ‰ for δD, Figure 9.B). This comparison of time series shows that thermal springs
518 at these two sites are neither influenced by the seasonal variations of rains nor by mixing with shallow
519 cold waters. The recharge, mostly influenced by important inputs of cyclonic water, is buffered by
520 multi-year infiltration. This suggests that the Salazie and Cilaos hydrothermal reservoirs, although
521 disconnected from each other, are sufficiently large and/or deep to be protected from superficial
522 perturbations.

523 *4.2.3.   Host rock*

524 In this section, we compared the $^{87}Sr/^{86}Sr$ in rocks and thermal waters to identify the geological units
525 hosting the hydrothermal system. As with the $\delta^{18}O$ and δD isotopic ratios, we observe that $^{87}Sr/^{86}Sr$
526 ratios are higher in the thermal springs of Salazie (0.704194 to 0.704364, mean 0.704276 ± 0.000047)
527 than in those of Cilaos (0.704129 to 0.704249, mean 0.704180 ± 0.000026), irrespective of Sr
528 concentrations (Table 1, Figure 10), as already mentioned by Sanjuan et al., (2001). Because there is
529 no fractionation between Sr isotopes during water-rock interaction, the strontium isotopic ratio is
530 preserved when Sr is leached from the rock by thermal waters. This dichotomy thus reflects a
531 difference between the two cirques in the $^{87}Sr/^{86}Sr$ ratios of rocks interacting with thermal fluids.

532 All rocks from Salazie and Cilaos (Table 3, Figure 10) fall in the range of $^{87}Sr/^{86}Sr$ ratios of thermal
533 springs (from 0.704086 to 0.704290), except for two outliers in Salazie (0.704041 and 0.704504).
534 However, our new analyses show that syenite intrusions, trachyte dykes and other differentiated
535 products fall in the lower range of this $^{87}Sr/^{86}Sr$ isotopic diversity (from 0.704153 to 0.704269, mean
536 0.704181), whether they come from Salazie, Cilaos, or from the summit. The comparison of rock and
537 thermal spring $^{87}Sr/^{86}Sr$ isotopic signatures thus strongly suggests that the hydrothermal fluids of Cilaos
538 interact with differentiated rocks at low $^{87}Sr/^{86}Sr$ isotopic ratios whereas those from Salazie interact
539 with more mafic rocks at higher $^{87}Sr/^{86}Sr$ isotopic ratios. Differentiated intrusions belong to the latest
540 volcanic activity of Piton des Neiges (150 to 27 ka), and thus represent the likeliest heat sources in the
541 edifice.

542
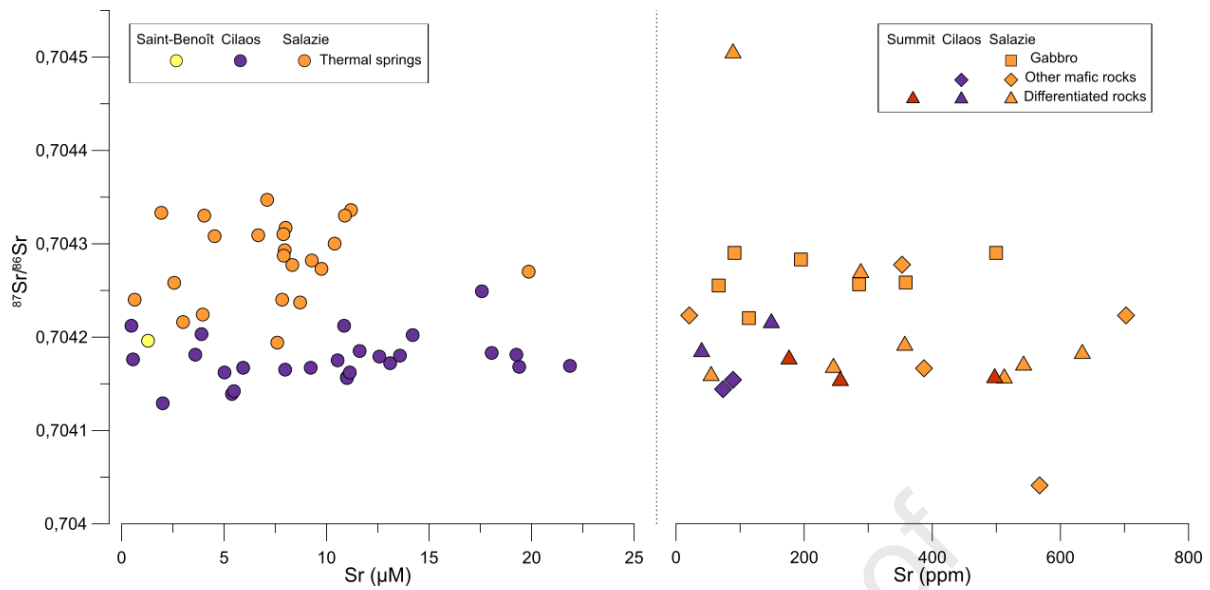
Figure 10: Strontium concentrations and [87]Sr/[86]Sr isotopic ratios in thermal springs (µmol/L) and rocks (ppm) from the cirques of Salazie and Cilaos.

Consequently, the contrasted [87]Sr/[86]Sr values of thermal springs of Salazie and Cilaos implies that the hydrothermal fluids interact with different rocks on the two sides of the summit. When combined with the contrasted $\delta^{18}O$ and δD signatures of thermal springs (Figure 11) which show that meteoric recharge is independent in the two cirques, we can deduce that the hydrothermal system is made of two reservoirs that do not mix with each other. The Cilaos reservoir, which shows more evidence of interaction with trachytes and syenites than the Salazie reservoir, is thus possibly closer to a heat source related to the terminal activity of Piton des Neiges, and is therefore more promising from a geothermal perspective.

25

553
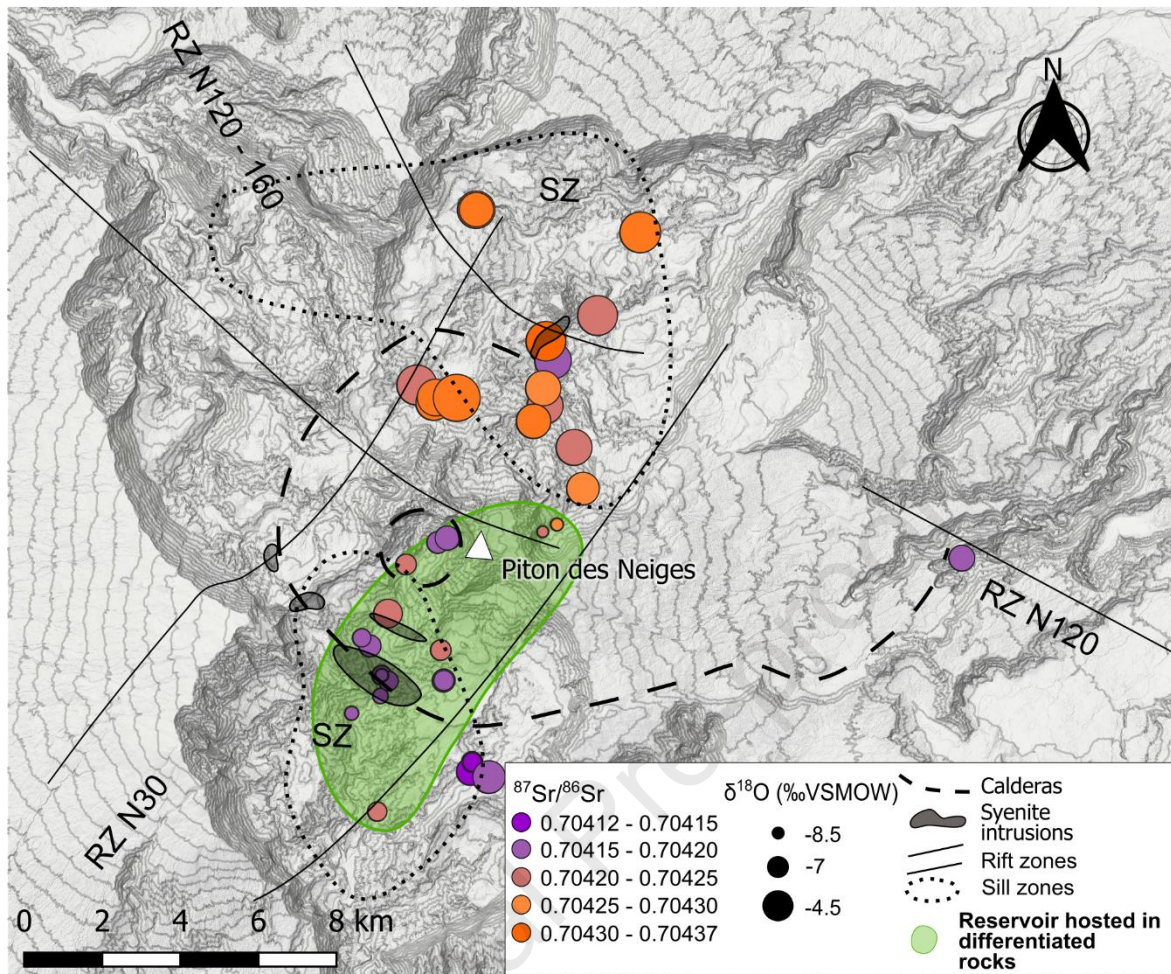
Figure 11: Spatial distribution of $\delta^{18}O$ (‰ VSMOW in symbol size) and $^{87}Sr/^{86}Sr$ (in color scale) in the thermal springs of Piton des Neiges. The green field represents the zone of lowest $^{87}Sr/^{86}Sr$ indicating an interaction of thermal waters with differentiated rocks, which may represent heat sources for the hydrothermal system. Volcano-tectonic structures (rift zones, sill zones, syenite intrusions, and calderas) are also represented.

558   4.3. Equilibration and geothermometry

559   The next step in the geochemical characterization of the resource is to provide a quantitative estimate
560   of the temperatures at which thermal waters and rocks interact. In a previous study, Sanjuan et al.,
561   (2001) proposed a reservoir temperature reaching 120-130°C, based on empirical and semi-empirical
562   geothermometers applied to the set of thermal springs known at that time. We now dispose of a wider
563   set of analyses of thermal springs. We chose to start our geothermometry study by selecting the
564   thermal springs most likely to have retained their reservoir characteristics. We then applied
565   multicomponent geothermometry and fluid reconstruction with a thermodynamic approach on this
566   selected subset of thermal springs to get an estimate of the reservoir conditions. The approach is
567   summarized below and detailed in Appendix B.

568   We compared outlet temperatures to the results of geothermometers for rapidly adjusting
569   equilibriums at low temperatures, such as K-Mg and amorphous silica systems (Fournier, 1977;
570   Fournier and Potter, 1979; Giggenbach, 1988), to assess the equilibrium state of thermal waters. The
571   closer the outlet temperature is to the temperatures obtained with these geothermometers, the more
572   re-equilibrated the waters are. We also used the values of the outlet temperatures as indicators of the
573   speed of transfer between the reservoir at depth and the surface. The higher the outlet temperatures

26

574 are, the faster the transfer and thus, the closer to reservoir conditions the waters are likely to be. Our
575 results show that the silica system is re-equilibrated for all springs, hence, equilibrium with silica will
576 have to be estimated for reservoir conditions in geothermometry computations. For the K-Mg systems
577 however, some springs are not fully re-equilibrated and may have retained some of their reservoir
578 characteristics. For geothermometry computation, we chose to select the five thermal springs that
579 displayed a > 20°C difference between their outlet temperatures and temperatures obtained with the
580 K-Mg geothermometer, as well as outlet temperatures higher than 25°C: BR16, BR17, RR1, TB and
581 OLIV2. Additionally, we selected thermal springs BR14 and BR12, whose K-Mg system are re-
582 equilibrated, but have the highest outlet temperatures (48.0 and 42.4°C, respectively). This selection
583 of analyses, based on outlet temperatures and geochemistry, corresponds to thermal springs found in
584 immediate vicinity of the syenite intrusions. This supports that syenite intrusions play the role as heat
585 sources and/or as drains channeling hydrothermal waters.

586 On these seven selected thermal springs, we performed multicomponent geothermometry using the
587 software iGeoT (Spycher and Finsterle, 2016), which couples the parameter estimation software
588 iTOUGH2 (Finsterle, 2007) with GeoT (Spycher et al., 2016). The principle is to find a temperature that
589 satisfies equilibrium between waters of a known composition and chosen reservoir minerals using
590 iterations of mass-balance/mass-action equations. Based on our previously acquired knowledge of the
591 hydrothermal system, we also modelled CO_2 loss and silica re-equilibration in our computations. For
592 thermal springs with several samples available (BR12, BR14, BR16, TB), the samples with the highest
593 equilibrium temperatures obtained with iGeoT are the less diluted, and hence those that we consider
594 as the most representative of reservoir conditions. The equilibrium temperatures obtained for this
595 selection of thermal springs are presented in Table 5. The uncertainties correspond to the T_{spread}
596 indicator of the iGeoT software, which gives the spread of log(Q/K) values for the selected minerals on
597 the temperature axis. Two examples of temperature estimations with iGeoT are shown in Figure 12
598 for the two highest temperatures obtained (springs BR12 and BR16).

599 Because the Na, K, and Ca activity ratios and the fugacity of CO_2 obtained with the model are all critical
600 parameters in the computation of the equilibrium temperatures, it is important to compare the results
601 of multi-equilibrium geothermometry with other geothermometers and geoindicators, such as those
602 from Fournier and Truesdell (1973), Giggenbach, (1984), and Cioni and Marini, (2020). The details of
603 this analysis are in section B.3 of the Supplementary material. We found that multi-equilibrium
604 geothermometry results are in discrepancy with the other geothermometers only for one sample of
605 spring BR14 and for three samples of spring BR16. In these samples, the equilibrium is likely disturbed
606 by an excess amount of CO_2 entering the system, which forces us to reject the temperatures deduced
607 from these analyses in our interpretation. For all the other samples, multi-equilibrium temperatures
608 and compositions obtained with iGeoT are in general consistency with other geothermometers and
609 geoindicators.

610 Table 5: Equilibrium temperatures obtained with geothermometry for selected analyses of thermal springs.

| Thermal spring	BR12	BR14	BR16	BR17	RR1	OLIV2	TB
Location	Cirque of Cilaos					Cirque of Salazie	
Equilibrium temperature (°C)	139	136	141	124	135	93	125
Uncertainty (T_{spread}, °C)	8	13	29	20	19	27	12
Confidence	Good	Medium	Medium	Good	Good	Good	Good

611
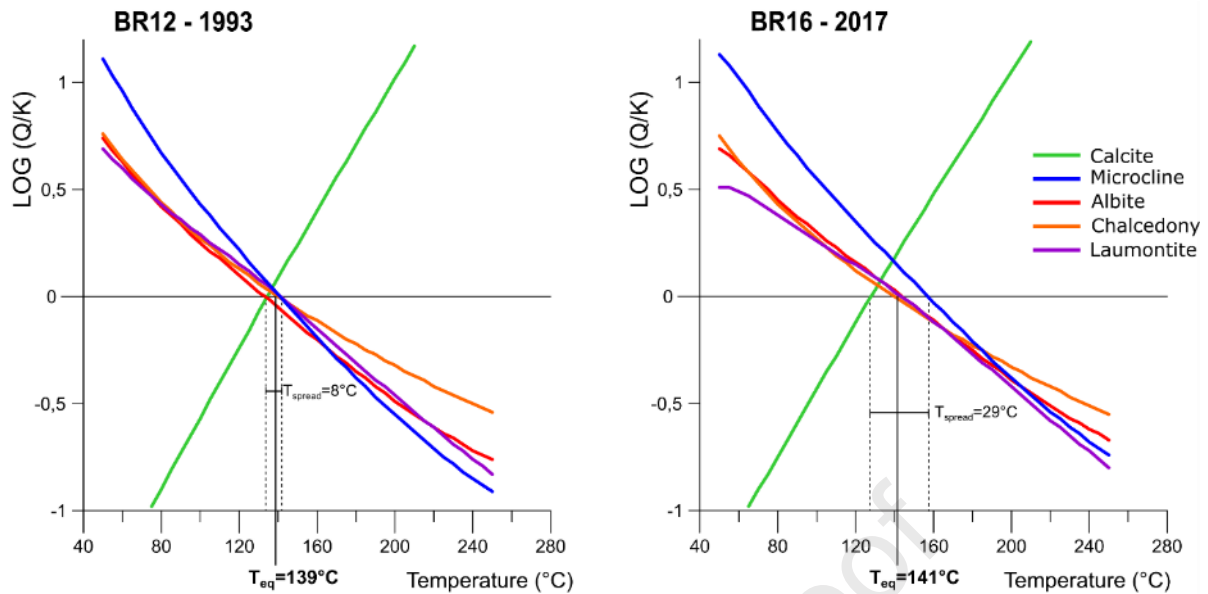
612

613 Figure 12: Examples of iGeoT computations on samples BR12 from Louvat and Allègre, (1997) and BR16 from
614 Bénard et al., (2020), represented as saturation indices (log(Q/K)) of reservoir minerals versus temperatures. Q is
615 the computed ion activity product with iGeoT and K the thermodynamic equilibrium constant of each mineral. The
616 clustering of log(Q/K) curves near zero gives the reservoir temperature (T_{eq}), weighted to take into account the
617 root-mean square, the standard deviation, the mean, and the scaled log(Q/K) absolute values. The uncertainty is
618 the spread of log(Q/K) values (T_{spread}) for all minerals on the temperature axis.

619 Our multi-equilibrium geothermometry approach yields equilibrium temperatures from 93 ± 14°C to
620 125 ± 6°C (weighted mean 120 ± 5°C) for the two selected springs in the cirque of Salazie, and from
621 124 ± 10°C to 141 ± 15°C (weighted mean 137 ± 3°C) for the five springs in Cilaos (Table 5). These results
622 are in general agreement with other geothermometers applied here and in Sanjuan et al., (2001,
623 section B.3 of the Supplementary material). This consistency of multiple geothermometers suggests
624 that the selected hydrothermal waters have reached equilibrium in their interaction with rock at the
625 obtained temperatures. These springs are the ones most likely to have retained reservoir
626 characteristics due to a fast transfer between the deep reservoir and the surface. It is important to
627 note that this equilibrium is only the last one that the hydrothermal waters may have experienced,
628 and that higher temperature equilibria may have occurred. In consequence, our results should be
629 considered as minimum temperatures for the two independent hydrothermal systems of Salazie and
630 Cilaos. Keeping this in mind, more thermal springs have reached equilibrium in Cilaos than in Salazie
631 (5 against 2), and the Cilaos hydrothermal system appears to have reached slightly higher minimum
632 temperatures than that of Salazie (Figure 13). In terms of geothermal resource, minimum equilibrium
633 temperatures are thus more favorable in the cirque of Cilaos than in Salazie.

634
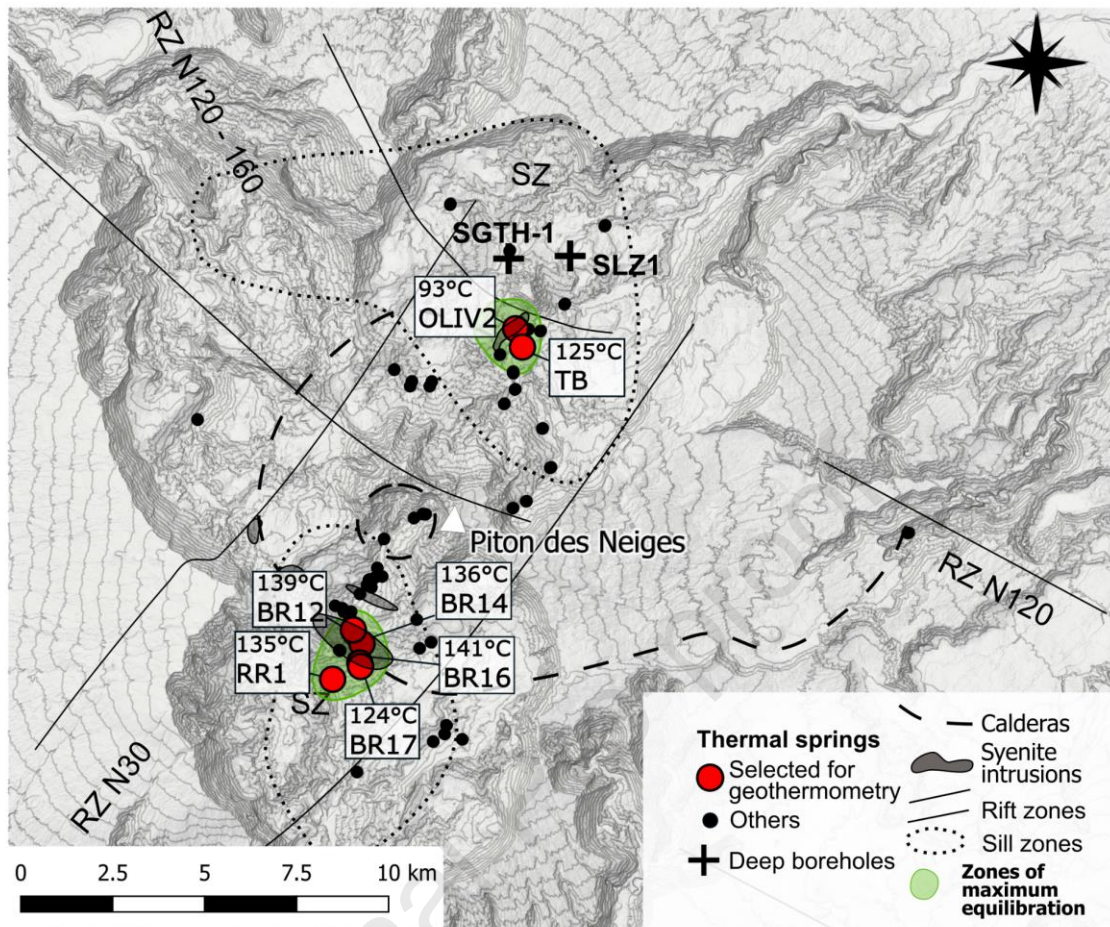
Figure 13: Spatial distribution of the thermal springs showing the best evidence of preserved high-temperature
equilibrium, and their multi-equilibrium temperature computed using iGeoT. relative to volcano-tectonic structures
(rift zones, sill zones, calderas). The green field represents the zone of highest equilibrium temperature of water-
rock interaction as defined in text. Volcano-tectonic structures (rift zones, sill zones, syenite intrusions, and
calderas) are also represented.

4.4. Geothermal resource

Our work has led us to identify zones where the geothermal resource appears to be the most promising
according to different criteria:

- 1. Maximum temperature and electrical conductivity in thermal springs,
- 2. Maximum degassing of CO_2,
- 3. Maximum contamination by seawater Cl, indicating that the hydrothermal system there is
  deeply rooted,
- 4. Compartmented reservoir which is hosted in late stage differentiated rocks that could be a
  heat source,
- 5. Most preserved equilibrium between thermal springs and the reservoir host rocks,
- 6. Minimum reservoir temperature of 130°C.

Figure 14 is a summary map superimposing all these six zones and thus giving the most probable
location of the geothermal resource. Two most promising zones are highlighted, one in the cirque of
Cilaos and the second is in the cirque of Salazie. This supports the observations made from the study

29

654 of the recharge and host rocks that there are two unconnected hydrothermal systems. These two
655 promising zones are located in the immediate surroundings of syenite intrusions, themselves located
656 at the junction of the N30°E rift zone and the supposed caldera of Piton des Neiges. This spatial
657 repartition clearly indicates that the differentiated magmas intruded in the N30°E rift zone during the
658 last activity of Piton des Neiges (150 – 27 ka, Famin et al., 2022), and to which the syenites belong,
659 represent the likeliest heat source of the two hydrothermal systems. The caldera structures and the
660 syenite intrusions could also represent preferential pathways for the ascent of hydrothermal fluids,
661 from a depth corresponding at least to the seawater level according to the slight contamination of
662 some springs by elements originating from seawater. The two hydrothermal systems appear large
663 and/or isolated enough to maintain a stable geochemical composition over several years.

664 The Cilaos zone is a more promising geothermal resource than the Salazie zone. This is partly due to
665 the higher average temperature obtained for the Cilaos reservoir (137 ± 3°C) compared to the Salazie
666 reservoir (125 ± 5°C). Additionally, the $^{87}Sr/^{86}Sr$ ratios of thermal springs from Cilaos, contrary to those
667 from Salazie, indicate that the thermal waters are interact with differentiated rocks that probably
668 constitute the heat source.

669 It is worth noting that in both cirques, the reservoir temperature estimates are below the limit of a
670 conventional energy-producing geothermal exploitation, which requires water at 150°C at the head of
671 the geothermal well (Moore and Simmons, 2013). We recall, however, that our estimates are minimum
672 temperatures of water-rock interaction, for hydrothermal waters that reach the surface. It is thus likely
673 that hotter hydrothermal waters exist at depth in the edifice, but either do not reach the surface or
674 are re-equilibrated at low temperature during their ascent.

675
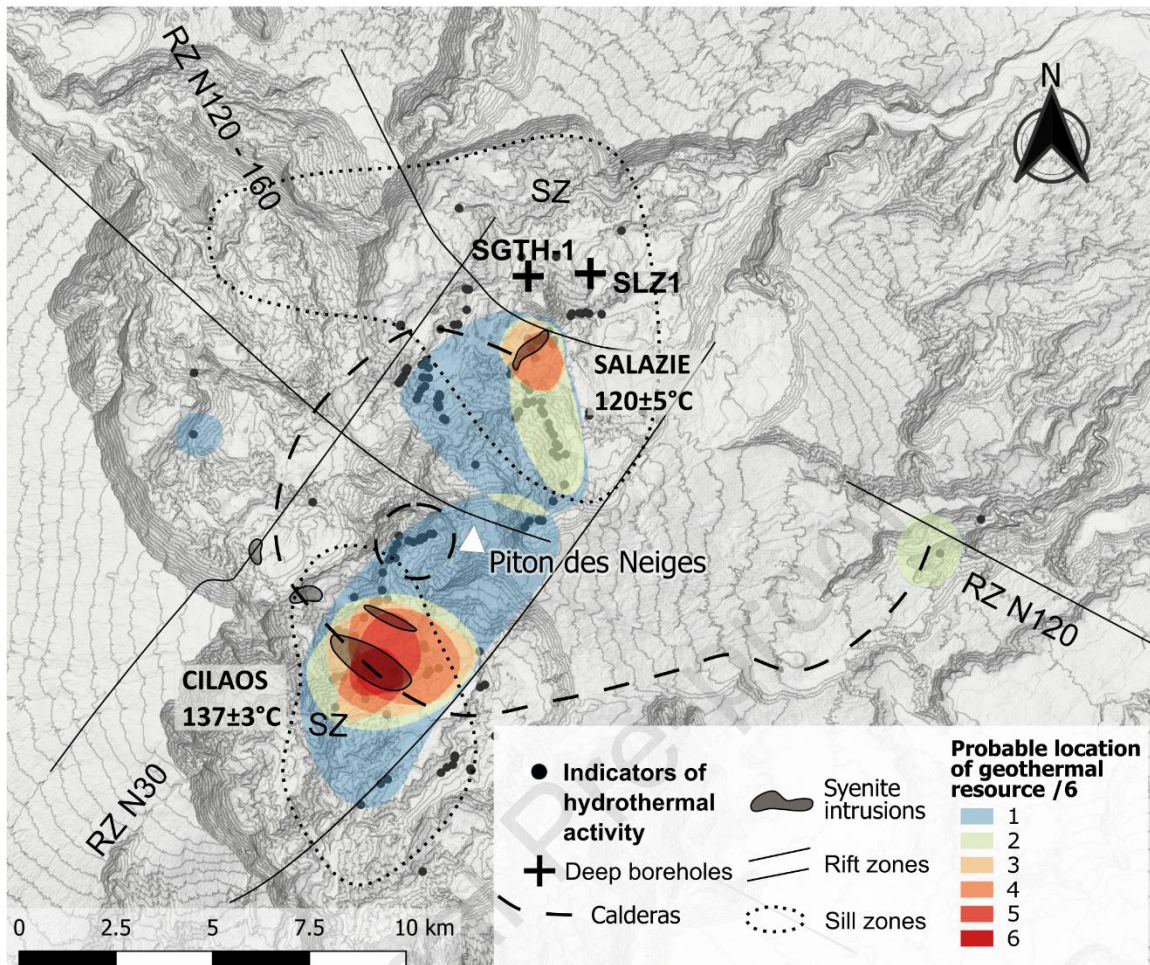
Figure 14: Superimposition of zones of: high temperature and electrical conductivity, high partial pressure of CO_2, high seawater contribution relative other thermal springs (meaning that waters circulated deep), strontium isotopic ratios corresponding to interaction with rocks from the late stage geological units, occurrence of thermal springs equilibrated with their reservoir host rock, and equilibrium temperatures of water-rock interaction of thermal springs superior to 130°C. The colors scale (/6) reflects how many zones are superimposed. The larger the number of superimposed zones, the most probable it is that there is a geothermal resource.

Conclusion

Our vast exploration campaign and our extended dataset in space and time of major, trace elements analyses and $\delta^{18}O$, δD, and $^{87}Sr/^{86}Sr$ isotopic ratios of thermal springs, rainwaters and rocks, allows us to significantly precise the location of the geothermal resource of Piton des Neiges volcano, to estimate a minimum temperature and to characterize its recharge. We show that the density of hydrothermal indicators, including thermal springs and dry sulfur, iron oxide, and carbonate deposits, is dramatically higher in the cirques of Salazie and Cilaos, along a N30°E axis corresponding to one of the volcanic rift zones of the edifice. Dry deposits, particularly abundant on the northern extremity of this axis, may represent the northern limit of hydrothermal activity. This may explain why previous investigation boreholes located north of Salazie encountered heat but no sufficient water yield.

Contrasted $\delta^{18}O$, δD, and $^{87}Sr/^{86}Sr$ signatures in and Salazie and Cilaos thermal springs show that Piton des Neiges hosts in fact two unconnected hydrothermal reservoirs, with independent meteoric recharges and different water-rock interactions. For these two reservoirs, the most promising geothermal resource in centered on syenite intrusions from the late stage magmatic activity. These

31

696 structures appear to be the likeliest heat source of hydrothermal activity, but also a preferential
697 pathway for the upward circulation of hot fluids. Thermal springs in the vicinity of these zones keep a
698 constant stable isotopic composition despite annual variations in rains. The recharge is multi-year,
699 mostly due to cyclones and tropical storms. This buffering capacity indicates large aquifer volumes
700 compared to annual infiltrations. The two hydrothermal aquifers display a slight seawater
701 contamination, which suggest that hot fluids rise from depths equal to or greater than sea level. Multi-
702 equilibrium geothermometry of selected thermal springs allow us to estimate a minimum temperature
703 of 125 ± 5°C for the Salazie hydrothermal system, and a slightly higher minimum temperature of 137
704 ± 3°C for Cilaos.

705 Our spatial and temporal investigation of geochemical parameters in thermal springs lead us to
706 considerably refine the characterization of the geothermal resource compared to previous studies. In
707 particular, intersections of major volcano-tectonic structures such as the N30°E rift zones, the trace of
708 the supposed caldera and syenites intrusions represent preferential targets for future investigations,
709 which should prioritize the cirque of Cilaos.

710 Our spatial and temporal visualization of the geochemical information is thus well suited for
711 geothermal exploration for geothermal systems with thermal springs strongly affected by mixing and
712 re-equilibration. This geochemical exploration methodology is applicable to any volcano as long as the
713 hydrothermal system leaks to the surface.

714 Acknowledgments

721 References

722 Appelo, C.A.J., Postma, D., 2005. Geochemistry, Groundwater and Pollution, 2nd Edition. ed. A.A.
723   Balkema Publishers.
724 Arnórsson, S., 1995. Geothermal systems in Iceland: Structure and conceptual models—II. Low-
725   temperature areas. Geothermics 24, 603–629. https://doi.org/10.1016/0375-6505(95)00026-
726   7
727 Assayag, N., Rivé, K., Ader, M., Jézéquel, D., Agrinier, P., 2006. Improved method for isotopic and
728   quantitative analysis of dissolved inorganic carbon in natural water samples. Rapid Commun.
729   Mass Spectrom. 20, 2243–2251. https://doi.org/10.1002/rcm.2585
730 Augé, T., Lerebour, P., Rançon, J.-P., 1989. The Grand Brûlé exploration drilling: New data on the deep
731   framework of the Piton de la Fournaise volcano. Part 3: Mineral chemistry of the cumulate
732   rocks. J. Volcanol. Geotherm. Res. 36, 139–151. https://doi.org/10.1016/0377-
733   0273(89)90010-3
734 Aunay, B., Dewandel, B., Ladouche, B., Oliva, Z., Saussol, P., 2012. Identification des modalités
735   d'exploitation des ressources en eaux souterraines du domaine d'altitude de l'Est de La
736   Réunion – Phase 3 (secteur des Plaines) (Rapport final No. RP-59245-FR
737   (http://infoterre.brgm.fr/rapports/RP-59245-FR.pdf)). BRGM.
738 Aunay, B., Gourcy, L., 2007. Approche hydrogéochimique pour la détermination de l'origine de la
739   contamination des eaux. (No. RP-55535-FR http://infoterre.brgm.fr/rapports//RP-55535-
740   FR.pdf). BRGM.

32

Aunay, B., Lucas, C., Ladouche, B., Vigouroux, P., Belle, P., 2013. Identification du potentiel en eau minérale gazeuse du cirque de Salazie (Rapport final No. RC-62181-FR). BRGM.

Ball, J.W., Nordstrom, D.K., 1991. User's manual for WATEQ4F, with revised thermodynamic data base and text cases for calculating speciation of major, trace, and redox elements in natural waters. US Geological Survey.

Belle, P., 2014. Contribution des processus hydrologiques et hydrogéologiques aux glissements de terrain de grande ampleur. Application au contexte tropical de La Réunion. Université de La Réunion, Saint-Denis, La Réunion.

Bénard, B., Famin, V., Agrinier, P., Aunay, B., Lebeau, G., Sanjuan, B., Vimeux, F., Bardoux, G., Dezayes, C., 2020. Origin and fate of hydrothermal fluids at Piton des Neiges volcano (Réunion Island): A geochemical and isotopic (O, H, C, Sr, Li, Cl) study of thermal springs. J. Volcanol. Geotherm. Res. 392, 106682. https://doi.org/10.1016/j.jvolgeores.2019.106682

Berthod, C., 2016. Relations entre systèmes intrusifs et instabilités sur un volcan basaltique (Piton des Neiges, La Réunion) (thesis). La Réunion.

Bird, D.K., Norton, D.L., 1981. Theoretical prediction of phase relations among aqueous solutions and minerals: Salton Sea geothermal system. Geochim. Cosmochim. Acta 45, 1479–1494. https://doi.org/10.1016/0016-7037(81)90280-5

Boudoire, G., Liuzzo, M., Di Muro, A., Ferrazzini, V., Michon, L., Grassa, F., Derrien, A., Villeneuve, N., Bourdeu, A., Brunet, C., Giudice, G., Gurrieri, S., 2017. Investigating the deepest part of a volcano plumbing system: Evidence for an active magma path below the western flank of Piton de la Fournaise (La Réunion Island). J. Volcanol. Geotherm. Res. 341, 193–207. https://doi.org/10.1016/j.jvolgeores.2017.05.026

Boudoire, G., Rizzo, A.L., Di Muro, A., Grassa, F., Liuzzo, M., 2018. Extensive CO 2 degassing in the upper mantle beneath oceanic basaltic volcanoes: First insights from Piton de la Fournaise volcano (La Réunion Island). Geochim. Cosmochim. Acta 235, 376–401. https://doi.org/10.1016/j.gca.2018.06.004

Bret, L., 2002. Minéralogie et géochimie des séries anciennes du Piton des Neiges : Modélisation et implications hydrogéologiques (Thèse). Université de la Réunion.

Chaput, M., Famin, V., Michon, L., 2017. Sheet intrusions and deformation of Piton des Neiges, and their implication for the volcano-tectonics of La Réunion. Tectonophysics 717, 531–546. https://doi.org/10.1016/j.tecto.2017.08.039

Chaput, M., Pinel, V., Famin, V., Michon, L., Froger, J.-L., 2014. Cointrusive shear displacement by sill intrusion in a detachment: A numerical approach. Geophys Res Lett 41 1937–1943.

Chevalier, L., 1979. Structures et évolution du volcan Piton des Neiges. Ile de la Réunion. Leurs relations avec les structures du bassin des Mascareignes. Océan indien occidental (Thèse). Université scientifique et médicale de Grenoble.

Chovelon, P., 1986. Forage géothermique de Salazie (SLZ1). Étude géologique du forage et dossier des ouvrages exécutés. (No. N°86CFG018).

Cioni, R., Marini, L., 2020. The Activity-Based Theoretical K–Ca and Na–Ca Geoindicators, in: Cioni, R., Marini, L. (Eds.), A Thermodynamic Approach to Water Geothermometry, Springer Geochemistry. Springer International Publishing, Cham, pp. 365–407. https://doi.org/10.1007/978-3-030-54318-1_8

Coudrain-Ribstein, A., Gouze, P., de Marsily, G., 1998. Temperature-carbon dioxide partial pressure trends in confined aquifers. Chem. Geol. 145, 73–89. https://doi.org/10.1016/S0009-2541(97)00161-7

Demange, J., Chovelon, P., Puvilland, P., 1989. Geothermal model of the Salazie Cirque (Reunion Island): Volcanic and structural implications. J. Volcanol. Geotherm. Res. 36, 153–176. https://doi.org/10.1016/0377-0273(89)90011-5

Dezayes, C., Famin, V., Tourlière, B., Baltassat, J.-M., Bénard, B., 2022. Potential areas of interest for the development of geothermal energy in La Réunion Island based on GIS analysis. J. Volcanol. Geotherm. Res. 421, 107450. https://doi.org/10.1016/j.jvolgeores.2021.107450

792 Di Paolo, F., Ledo, J., Slezak, K., Martínez van Dorth, D., Cabrera Pérez, I., Pérez, N., 2020. La Palma
793   island (Spain) geothermal system revealed by 3D magnetotelluric data inversion. Sci. Rep. 10,
794   18181. https://doi.org/10.1038/s41598-020-75001-z

795 Dumont, M., Reninger, P.A., Pryet, A., Martelet, G., Aunay, B., Join, J.L., 2018. Agglomerative
796   hierarchical clustering of airborne electromagnetic data for multi-scale geological studies. J.
797   Appl. Geophys. 157, 1–9. https://doi.org/10.1016/j.jappgeo.2018.06.020

798 Famin, V., Berthod, C., Michon, L., Eychenne, J., Brothelande, E., Mahabot, M.-M., Chaput, M., 2016.
799   Localization of magma injections, hydrothermal alteration, and deformation in a volcanic
800   detachment (Piton des Neiges, La Réunion). J. Geodyn., Fluids in crustal deformation : fluid
801   flow, fluid-rock interactions, rheology, melting and resources 101, 155–169.
802   https://doi.org/10.1016/j.jog.2016.05.007

803 Famin, V., Paquez, C., Danišík, M., Gardiner, N.J., Michon, L., Kirkland, C.L., Berthod, C., Friedrichs, B.,
804   Schmitt, A.K., Monié, P., 2022. Multi-technique Geochronology of Intrusive and Explosive
805   Activity on Piton des Neiges Volcano, Réunion Island. Geochem. Geophys. Geosystems n/a,
806   e2021GC010214. https://doi.org/10.1029/2021GC010214

807 Finsterle, S., 2007. iTOUGH2 user's guide. Earth Sci. Div. Lawrence Berkeley Natl. Lab. Univ. Calif.
808   Berkeley CA Httpwww-Esd Lbl GovTOUGHmanualsiTOUGH2GSLIBUsersGuide Pdf.

809 Fournier, R.O., 1977. Chemical geothermometers and mixing models for geothermal systems.
810   Geothermics 5, 41–50. https://doi.org/10.1016/0375-6505(77)90007-4

811 Fournier, R.O., Potter, R.W., 1979. Magnesium correction to the Na⬚K⬚Ca chemical geothermometer.
812   Geochim. Cosmochim. Acta 43, 1543–1550. https://doi.org/10.1016/0016-7037(79)90147-9

813 Fournier, R.O., Truesdell, A.H., 1973. An empirical Na-K-Ca geothermometer for natural waters.
814   Geochim. Cosmochim. Acta 37, 1255–1275. https://doi.org/10.1016/0016-7037(73)90060-4

815 Frissant, N., Gourcy, L., Brach, M., 2005. Recherche d'une relation entre le plateau de Dos-d'Ane et les
816   sources Blanche et Denise (No. RP-54167-FR (http://infoterre.brgm.fr/rapports/RP-54167-
817   FR.pdf)). BRGM.

818 Frissant, N., Lacquement, F., Rançon, J.P., 2003. Etude du potentiel hydrothermal de la zone amont de
819   la rivière du Bras Rouge (Cirque de Cilaos) -Première phase d'étude- (No. RP-52673-FR
820   (http://infoterre.brgm.fr/rapports/RP-52673-FR.pdf)). BRGM.

821 Gérard, A., Stieltjes, L., 1979. Evaluation du potentiel géothermique de l'île de La Réunion. 2ème phase
822   exploratoire: géologie et géophysique. (No. 79SGN538GTH).

823 Giggenbach, W.F., 1988. Geothermal solute equilibria. Derivation of Na-K-Mg-Ca geoindicators.
824   Geochim. Cosmochim. Acta 52, 2749–2765. https://doi.org/10.1016/0016-7037(88)90143-3

825 Giggenbach, W.F., 1984. Mass transfer in hydrothermal alteration systems—A conceptual approach.
826   Geochim. Cosmochim. Acta 48, 2693–2711. https://doi.org/10.1016/0016-7037(84)90317-X

827 Gillot, P.-Y., Nativel, P., 1982. K-Ar chronology of the ultimate activity of piton des neiges volcano,
828   reunion island, Indian ocean. J. Volcanol. Geotherm. Res. 13, 131–146.
829   https://doi.org/10.1016/0377-0273(82)90024-5

830 Grasby, S., Ansari, S., Calahorrano-Di Patre, A., Chen, Z., Craven, J., Dettmer, J., Gilbert, H., Hanneson,
831   C., Harris, M., Liu, J., others, 2019. Geothermal Resource Potential of the Garibaldi Volcanic
832   Belt, Southwestern British Columbia (Part of NTS 092J). Geosci. BC Summ. Act. 2020–02.

833 Grunberger, O., 1989. Etude géochimique et isotopique de l'infiltration sous climat tropical contrasté.
834   Massif du Piton des Neiges. Ile de la Réunion (Thèse). Université de Paris XI.

835 Gudmundsson, B.T., Arnórsson, S., 2005. Secondary mineral–fluid equilibria in the Krafla and Námafjall
836   geothermal systems, Iceland. Appl. Geochem. 20, 1607–1625.
837   https://doi.org/10.1016/j.apgeochem.2005.04.020

838 Gunnlaugsson, E., Arnòrsson, S., 1982. The chemistry of iron in geothermal systems in iceland. J.
839   Volcanol. Geotherm. Res. 14, 281–299. https://doi.org/10.1016/0377-0273(82)90066-X

840 Herrera, C., Custodio, E., 2014. Groundwater flow in a relatively old oceanic volcanic island: The
841   Betancuria area, Fuerteventura Island, Canary Islands, Spain. Sci. Total Environ. 496, 531–550.
842   https://doi.org/10.1016/j.scitotenv.2014.07.063

843   IAEA/WMO, 2019. Global Network of Isotopes in Precipitation. The GNIP Database. Accessible at:
844   http://www.iaea.org/water.
845   Iundt, F., Mauroux, B., Barrera, L., Cruchet, M., Martignoni, P., Stieltjes, L., 1992. Etude des sources
846   thermominérales de Cilaos (No. RR-35833-FR). BRGM.
847   Join, J.-L., Folio, J.-L., Robineau, B., 2005. Aquifers and groundwater within active shield volcanoes.
848   Evolution of conceptual models in the Piton de la Fournaise volcano. J. Volcanol. Geotherm.
849   Res. 147, 187–201. https://doi.org/10.1016/j.jvolgeores.2005.03.013
850   Jumaux, G., Queletard, H., Roy, D., 2011. Atlas climatique de la Réunion. METEOFRANCE.
851   Kluska, J.M., 1997. Evolution magmatique et morpho-structurale du Piton des Neiges au cours des
852   derniers 500000 ans (Thèse). Université de Paris 11, Orsay.
853   Kristmannsdóttir, H., 1983. Chemical evidence from Icelandic geothermal systems as compared to
854   submarine geothermal systems, in: Hydrothermal Processes at Seafloor Spreading Centers.
855   Springer, pp. 291–320.
856   Kristmannsdottir, H., 1979. Alteration of Basaltic Rocks by Hydrothermal-Activity at 100-300°C, in:
857   Mortland, M.M., Farmer, V.C. (Eds.), Developments in Sedimentology, International Clay
858   Conference 1978. Elsevier, pp. 359–367. https://doi.org/10.1016/S0070-4571(08)70732-5
859   Lautze, N., Thomas, D., Hinz, N., Apuzen-Ito, G., Frazer, N., Waller, D., 2017a. Play fairway analysis of
860   geothermal resources across the State of Hawaii: 1. Geological, geophysical, and geochemical
861   datasets. Geothermics 70, 376–392. https://doi.org/10.1016/j.geothermics.2017.02.001
862   Lautze, N., Thomas, D., Waller, D., Frazer, N., Hinz, N., Apuzen-Ito, G., 2017b. Play fairway analysis of
863   geothermal resources across the state of Hawaii: 3. Use of development viability criterion to
864   prioritize   future   exploration   targets.   Geothermics   70,   406–413.
865   https://doi.org/10.1016/j.geothermics.2017.07.005
866   Liuzzo, M., Di Muro, A., Giudice, G., Michon, L., Ferrazzini, V., Gurrieri, S., 2015. New evidence of CO2
867   soil degassing anomalies on Piton de la Fournaise volcano and the link with volcano tectonic
868   structures.   Geochem.   Geophys.   Geosystems   16,   4388–4404.
869   https://doi.org/10.1002/2015GC006032
870   Lopoukhine, M., Stieltjes, L., 1978. Evaluation du Potentiel géothermique de l'Île de la Réunion - 1ère
871   Phase exploratoire : Géologie et géochimie des eaux (No. 78 SGN 467 GTH). BRGM.
872   Louvat, P., Allègre, C.J., 1997. Present denudation rates on the island of Réunion determined by river
873   geochemistry: Basalt weathering and mass budget between chemical and mechanical
874   erosions. Geochim. Cosmochim. Acta 61, 3645–3669. https://doi.org/10.1016/S0016-
875   7037(97)00180-4
876   Manès, G. (1871-) A. du texte, n.d. La Réunion : sanatoria, tourisme, livret-guide, illustré / par le
877   docteur G. Manès,...
878   Marty, B., Meynier, V., Nicolini, E., Griesshaber, E., Toutain, J.P., 1993. Geochemistry of gas
879   emanations: A case study of the Réunion Hot Spot, Indian Ocean. Appl. Geochem. 8, 141–152.
880   https://doi.org/10.1016/0883-2927(93)90030-K
881   McDougall, I., 1971. The geochronology and evolution of the young volcanic island of Réunion, Indian
882   Ocean.   Geochim.   Cosmochim.   Acta   35,   261–288.   https://doi.org/10.1016/0016-
883   7037(71)90037-8
884   Mook, W.G., Koene, B.K.S., 1975. Chemistry of dissolved inorganic carbon in estuarine and coastal
885   brackish   waters.   Estuar.   Coast.   Mar.   Sci.   3,   325–336.   https://doi.org/10.1016/0302-
886   3524(75)90032-8
887   Moore,   J.N.,   Simmons,   S.F.,   2013.   More   Power   from   Below.   Science   340,   933–934.
888   https://doi.org/10.1126/science.1235640
889   Nauret, F., Famin, V., Vlastélic, I., Gannoun, A., 2019. A trace of recycled continental crust in the
890   Réunion hotspot. Chem. Geol. 524, 67–76. https://doi.org/10.1016/j.chemgeo.2019.06.009
891   Palandri, J.L., Reed, M.H., 2001. Reconstruction of in situ composition of sedimentary formation
892   waters.   Geochim.   Cosmochim.   Acta   65,   1741–1767.   https://doi.org/10.1016/S0016-
893   7037(01)00555-5

894 Pang, Z.-H., Reed, M., 1998. Theoretical Chemical Thermometry on Geothermal Waters: Problems and
895   Methods. Geochim. Cosmochim. Acta 62, 1083–1091. https://doi.org/10.1016/S0016-
896   7037(98)00037-4
897 Petit, V., Dewandel, B., Charlier, J.B., Ollivier, P., Lucas, C., Oliva, Z., 2013. Amélioration de la
898   connaissance hydrogéologique de l'aquifère côtier du Gol. (No. RP-61834-FR
899   http://infoterre.brgm.fr/rapports//RP-61834-FR.pdf). BRGM.
900 Poul, X., 1966. Les sources thermominérales de Cilaos étude géologique et étude des principales
901   caractéristiques : débit, température et résistivité-des captages existants. (No. 66- TAN- 027).
902   BRGM.
903 Rançon, J.P., Rocher, P., 1985. Découverte de zones fumerolliennes récentes dans le cirque de Salazie
904   (île de La Réunion, Océan Indien). C R Académie Sci. Sér. II 16, 821–826.
905 Rançon, J.Ph., 1985. Hydrothermal history of Piton des Neiges volcano (Reunion Island, Indian Ocean).
906   J. Volcanol. Geotherm. Res. 26, 297–315. https://doi.org/10.1016/0377-0273(85)90061-7
907 Reed, M., Palandri, J., 2006. SOLTHERM. H06, a database of equilibrium constants for minerals and
908   aqueous species. Available Authors.
909 Reed, M., Spycher, N., 1984. Calculation of pH and mineral equilibria in hydrothermal waters with
910   application to geothermometry and studies of boiling and dilution. Geochim. Cosmochim. Acta
911   48, 1479–1492. https://doi.org/10.1016/0016-7037(84)90404-6
912 Rocher, P., 1988. Contexte volcanique et structural de l'hydrothermalisme récent dans le massif du
913   Piton des neiges (île de La Réunion): étude détaillée du cirque de Salazie. s.n., S.l.
914 Sanjuan, B., Genter, A., Brach, M., Lebon, D., 2001. Compléments d'étude géothermique dans l'île de
915   la Réunion (géologie, géochimie) (No. RP-51189-FR (http://infoterre.brgm.fr/rapports/RP-
916   51189-FR.pdf)). BRGM.
917 Smietana, M., 2011. Petrology, geochronology (K-Ar) and elemental and isotopic geochemistry (Sr, Nd,
918   Hf, Pb) of older lavas of Reunion : Implications for the construction of the volcanic edifice
919   (Theses). Université de la Réunion.
920 Spycher, N., Finsterle, S., 2016. iGeoT v1.0: Automatic Parameter Estimation for Multicomponent
921   Geothermometry, User's Guide:
922 Spycher, N., Peiffer, L., Finsterle, S., Sonnenthal, E., 2016. GeoT User's Guide, A Computer Program for
923   Multicomponent Geothermometry and Geochemical Speciation, Version 2.1:
924 Troll, V.R., Carracedo, J.C., 2016. The geology of the Canary Islands. Elsevier.
925 Trull, T., Nadeau, S., Pineau, F., Polve´, M., Javoy, M., 1993. C-He systematics in hotspot xenoliths:
926   Implications for mantle carbon contents and carbon recycling. Earth Planet. Sci. Lett. 118, 43–
927   64. https://doi.org/10.1016/0012-821X(93)90158-6
928 Vesselinov, V.V., O'Malley, D., Frash, L.P., Ahmmed, B., Rupe, A.T., Karra, S., Middleton, R.S.,
929   Alexandrov, B., Mudunuru, M.K., Mims, M., Jameson, K., Sun, A., Scanlon, B., Banerji, A.,
930   Tartakovsky, D.M., Horne, R.N., Zhou, Z., Maguire, C., Skillman, S., Scharer, J., 2021. Geo
931   Thermal Cloud: Cloud Fusion of Big Data and Multi-Physics Models using Machine Learning for
932   Discovery, Exploration, and Development of Hidden Geothermal Resources. United States.
933   https://doi.org/10.2172/1782607
934

Declaration of interests

☒ The authors declare that they have no known competing financial interests or personal relationships that could have appeared to influence the work reported in this paper.

☐ The authors declare the following financial interests/personal relationships which may be considered as potential competing interests: